

# Neurogliaform Cells Exhibit Laminar-specific Responses in the Visual Cortex and Modulate Behavioral State-dependent Cortical Activity

**Gord Fishell**

[gordon\\_fishell@hms.harvard.edu](mailto:gordon_fishell@hms.harvard.edu)

Harvard University <https://orcid.org/0000-0002-9640-9278>

**Shuhan Huang**

Harvard Medical School <https://orcid.org/0000-0002-3139-7296>

**Daniella Rizzo**

Harvard Medical School And The Stanley Center At The Broad

**Sherry Wu**

Harvard Medical School And The Stanley Center At The Broad

**Qing Xu**

NYU Abu Dhabi <https://orcid.org/0000-0001-9479-470X>

**Leena Zaine**

Harvard Medical School And The Stanley Center At The Broad

**Norah Alghamdi**

King Abdullah University of Science and Technology

**David Stafford**

Berkeley University

**Tanya Daigle**

Allen Institute for Brain Science

**Bosiljka Tasic**

Allen Institute for Brain Science <https://orcid.org/0000-0002-6861-4506>

**Hongkui Zeng**

Allen Institute for Brain Science <https://orcid.org/0000-0002-0326-5878>

**Leena Ibrahim**

King Abdullah University of Science and Technology

---

**Article**

**Keywords:**

**Posted Date:** July 2nd, 2024

**DOI:** <https://doi.org/10.21203/rs.3.rs-4530873/v1>

**License:** © ⓘ This work is licensed under a Creative Commons Attribution 4.0 International License.

[Read Full License](#)

**Additional Declarations:** **Yes** there is potential Competing Interest. The senior author is a founder of Regel Therapeutics

---

# 1 Neurogliaform Cells Exhibit Laminar-specific Responses in the Visual Cortex and Modulate Behavioral State- 2 dependent Cortical Activity

3  
4 Shuhan Huang<sup>1,2,3</sup>, Daniella Rizzo<sup>1,3</sup>, Sherry Jingjing Wu<sup>1,3</sup>, Qing Xu<sup>4,5</sup>, Leena Ziane<sup>1,3</sup>, Norah Alghamdi<sup>4</sup>, David A.  
5 Stafford<sup>6</sup>, Tanya L. Daigle<sup>7</sup>, Bosiljka Tasic<sup>7</sup>, Hongkui Zeng<sup>7</sup>, Leena Ali Ibrahim<sup>4</sup> & Gord Fishell<sup>1,3</sup>

6 <sup>1</sup>Harvard Medical School, Blavatnik Institute, Department of Neurobiology, Boston, MA 02115, USA

7 <sup>2</sup>Program in Neuroscience, Harvard University, Cambridge, MA 02138, USA

8 <sup>3</sup>Stanley Center for Psychiatric Research, Broad Institute of MIT and Harvard, Cambridge, MA 02142, USA

9 <sup>4</sup>Biological and Environmental Sciences and Engineering Division, King Abdullah University of Science and Technology,  
10 Thuwal, 23955–6900, Kingdom of Saudi Arabia

11 <sup>5</sup>Past address: Center for Genomics & Systems Biology, New York University Abu Dhabi, Abu Dhabi, UAE

12 <sup>6</sup>Department of Molecular and Cell Biology, University of California, Berkeley, Berkeley, CA 94708, USA

13 <sup>7</sup>Allen Institute for Brain Science, Seattle, WA 98109, USA

## 14 **ABSTRACT**

15 Neurogliaform cells are a distinct type of GABAergic cortical interneurons known for their ‘volume transmission’ output  
16 property. However, their activity and function within cortical circuits remain unclear. Here, we developed two genetic tools  
17 to target these neurons and examine their function in the primary visual cortex. We found that the spontaneous activity of  
18 neurogliaform cells positively correlated with locomotion. Silencing these neurons increased spontaneous activity during  
19 locomotion and impaired visual responses in L2/3 pyramidal neurons. Furthermore, the contrast-dependent visual  
20 response of neurogliaform cells varies with their laminar location and is constrained by their morphology and input  
21 connectivity. These findings demonstrate the importance of neurogliaform cells in regulating cortical behavioral state-  
22 dependent spontaneous activity and indicate that their functional engagement during visual stimuli is influenced by their  
23 laminar positioning and connectivity.

## 25 **INTRODUCTION**

26 GABAergic cortical interneurons (cINs) play a crucial role in regulating cortical function through inhibition. Despite their  
27 relatively small numbers, these neurons are vital for controlling the activity of neuronal circuits, and their dysfunction can  
28 lead to a variety of neurological disorders. Over the past two decades, it has become recognized that they are comprised  
29 by four major cardinal types, which can be distinguished based on their expression of the molecular markers: parvalbumin

30 (PVALB), somatostatin (SST), vasoactive-intestinal peptide (VIP), and lysosome-associated membrane protein 5  
31 (LAMP5). Recent studies have extensively characterized their range of diversity, which is formed during development and  
32 results in each class possessing unique gene expression, morphologies, physiological properties, connectivities, and *in*  
33 *vivo* function<sup>1-5</sup>. Among the four cardinal types, LAMP5+ cINs have been the least investigated. This reflects the historic  
34 lack of genetic tools to specifically target them. Despite being initially discovered by Ramón y Cajal over 125 years ago<sup>6</sup>,  
35 their contribution to cortical function within neural circuits remains uncertain. In addition, it is unclear whether LAMP5+  
36 cINs residing in different layers exhibit distinct functional activities.

37 Neurogliaform cells, also referred to as dwarf, spiderweb, or arachniform cells in the literature, are classified as the  
38 LAMP5+ cardinal type cINs and constitute the majority of LAMP5+ cINs<sup>7-11</sup>. Despite exhibiting heterogeneous morphology  
39 within the population in accordance with their laminar location (they are elongated in layer 1 (L1) while spherical in layers  
40 2/3 (L2/3))<sup>12</sup>, neurogliaform cells share several commonalities in their dendritic and axonal organization<sup>1,12-17</sup>. They  
41 possess short, spherically-distributed and sparsely branched dendrites. Their axons are notably thin and form a highly  
42 ramified network within their cortical layer, occasionally extending into adjacent layers.

43 Neurogliaform cells exhibit a distinct late-spiking electrophysiological signature, characterized by a slow ramp of  
44 depolarization until the first spike occurs at rheobase<sup>12,13,18,19</sup>. Although their axonal varicosities contain synaptic vesicles,  
45 they seldom form conventional synaptic contacts and instead are thought to signal through 'volume transmission'<sup>17,18,20</sup>.  
46 Activation of neurogliaform cells induces slow and prolonged inhibitory postsynaptic potentials (IPSPs) in most adjacent  
47 neurons, mediated by extra-synaptically located GABAA and GABAB receptors<sup>14,18,21</sup>. Neurogliaform cells are electrically  
48 coupled to not only other neurogliaform cells but also other cIN types, suggesting they may monitor inhibitory network  
49 activity and regulate synchrony via gap junctions<sup>22-24</sup>.

50 Nevertheless, the *in vivo* activity and function of neurogliaform cells remain unclear. Given their 'volume transmission'  
51 output property that results in them mediating prolonged and non-selective broad inhibition, we hypothesize that these  
52 neurons suppress baseline cortical activity when recruited, and contribute to maintaining a high signal-to-noise ratio  
53 (SNR) in cortical function. Additionally, their short dendritic structure suggests that laminar-specific inputs selectively  
54 target these cINs within their respective layers.

55 In this study, we investigated the functional consequence of removing LAMP5+ cINs and compared their activity and  
56 connectivity across different cortical layers. Our goal was to (1) understand how LAMP5+ cINs are recruited during  
57 various behavioral states, and (2) determine whether these cINs in different cortical layers might be recruited differently in  
58 specific contexts. We used the primary visual cortex (V1) in mice as a model to address these questions. Firstly, we  
59 developed and validated two new genetic strategies enabling selective targeting of LAMP5+ cINs. Secondly, we silenced

LAMP5+ cINs, which led to increased spontaneous activity during locomotion, increased synchronization, and impaired visual responses in L2/3 pyramidal neurons (PYN<sup>L23</sup>) in V1. We also found that LAMP5+ cINs exhibited spontaneous activity that positively correlated with the animal's active behavioral states. Finally, we observed disparities in visually evoked responses between LAMP5+ cINs in L1 (LAMP5<sup>L1</sup>) and L2/3 (LAMP5<sup>L23</sup>). Specifically, while LAMP5<sup>L23</sup> showed a preference for high-contrast visual stimuli during locomotion, LAMP5<sup>L1</sup> preferred low-contrast visual stimuli. We investigated whether the circuit connectivity of LAMP5+ cINs in V1 explains these differences and found that the inputs to these neurons vary depending on their laminar location. In summary, our study introduced new tools for accessing this underexplored population, and revealed the recruitment and function of LAMP5+ cINs in cortical circuits.

## RESULTS

### Genetic Targeting of LAMP5+ cINs in Mouse V1.

Single cell RNA sequencing and spatial transcriptomic data<sup>10,25</sup> have revealed that the majority of LAMP5+ cINs express NPY (**Extended Data 1a1**), confirming their identity as neurogliaform cells described in previous literature<sup>6,11–13,18</sup>. Interestingly, among all cINs, these neurons also exhibited the highest expression of GAD2<sup>26,27</sup> (**Extended Data 1a2**), enabling them to exert powerful inhibition<sup>14,18</sup>. While many LAMP5+ cINs are located in L1, we estimate that ~60% of this cardinal type could reside in L2-6 (**Figure 1a**). To date, *in vivo* studies of LAMP5+ cINs have primarily focused on those within L1<sup>28–32</sup>, however, considerably less attention has been given to those in the other cortical layers<sup>33</sup>. This is largely because we currently lack genetic tools to access LAMP5<sup>L2-6</sup>.

To address this issue, we developed and validated two genetic labeling strategies to label all LAMP5+ cINs within the mouse V1. In the first strategy, *DLX-Cre; LAMP5-FlpO* alleles were bred with an intersectional reporter *Ai65(RCFL-tdT)* (**Figure 1b**). While LAMP5 is primarily restricted to LAMP5+ cINs, it is also expressed within a subset of excitatory neurons. The use of the *DLX-Cre* allele restricted the expression to cINs, and the *LAMP5-FlpO* allele limited it to the LAMP5+ cIN population. Our genetic labeling strategy demonstrated that LAMP5+ cINs are primarily enriched within L1 and L2/3 (~42.5% in L1 and ~38% in L2/3) (**Figure 1b-d**)<sup>10,12</sup>. Notably, although the level of neurite fluorescence was equivalent across L2/3 (**Figure 1d**), the density of labeled cell bodies was higher in L2 than in L3 (**Figure 1c**). By contrast, significantly fewer cells were observed in L4-6 (~19.5%), accompanied by the lowest intensity of neurite fluorescent signals in L5 (**Figure 1c,d, Extended Data 1b**).

To validate the specificity of this targeting strategy, we examined the colocalization between the genetically labeled neurons and marker genes we identified for LAMP5+ cINs using RNAscope. Over 95% of the labeled neurons were

88 DLX1+ (**Extended Data 1d**), confirming their identity as cINs. Moreover, most of the labeled neurons express NPY (80%  
89 in L1, 93-100% in L2-6, **Figure 1e**) and SV2C (90% in L1 and 98-100% in L2-6, **Figure 1f**), markers enriched in  
90 neurogliaform cells. The distribution of two other markers, LSP1 (7% in L1, 49% in L2/3, 74-83% in L4-6, **Figure 1g**) and  
91 NDNF (85% in L1, 10% in L2/3, 6% in L4-6, **Figure 1h**), was consistent with distinct LAMP5+ cIN subtypes in L2-6 and  
92 L1, respectively. These results aligned with the expected ratios from transcriptomic data. Additionally, almost all SV2C+  
93 cells in L1-4 (**Extended Data 1c1**) and NDNF+ cells in L1-3 (**Extended Data 1c2**) were labeled, underscoring the  
94 robustness of this targeting strategy. To rule out nonspecific labeling in other cIN types, we assessed co-expression with  
95 LHX6 (detects PV+ and SST+ cINs), VIP and SNCG, and observed minimal overlap (**Extended Data 1e-g**). Furthermore,  
96 the distribution of LAMP5+ cINs appears similar across different neocortical regions, including the primary somatosensory  
97 cortex (SSp) barrel field (**Extended Data 1h-j**) and the primary motor cortex (MOp) (**Extended Data 1k-m**). Collectively,  
98 these results suggest that the *DLX-Cre; LAMP5-FlpO* offers specific and robust access to the LAMP5+ cIN population.

99 While the intersectional *DLX-Cre; LAMP5-FlpO* provides comprehensive genetic access to LAMP5+ cINs, the requirement  
100 for multiple alleles reduces its flexibility. Therefore, we devised an alternative strategy using a single allele, *JAM2-Cre*, in  
101 conjunction with local viral delivery of Cre-dependent AAV driven by *Dlx* enhancer<sup>34</sup> (**Extended Data 2a**). This approach  
102 allows for selective targeting of LAMP5+ cINs in adults (**Extended Data 2b**; see Method - Mouse). We assessed the  
103 specificity of this targeting using similar methods. Labeled neurons co-express GAD2 (100%, **Extended Data 2c**), NPY  
104 (82% in L1, 81% in L2/3, 100% in L4-5, 86% in L6, **Extended Data 2d**), SV2C (76-80%, **Extended Data 2e**), LSP1 (4.5%  
105 in L1, 60-67% in L2-6, **Extended Data 2f**) and NDNF (82% in L1, **Extended Data 2g**), suggesting this strategy closely  
106 mirrors the LAMP5+ cIN labeling achieved with *DLX-Cre; LAMP5-FlpO* approach. As expected, a large proportion of the  
107 targeted neurons exhibited late-spiking electrophysiological characteristics, a trait associated with neurogliaform cells  
108 (**Extended Data 2i**)<sup>35</sup>. These neurons also displayed typical neurogliaform cell morphology with short spherical dendrites  
109 and thin, highly ramified axons (**Extended Data 2j**)<sup>12</sup>. Off-target analysis revealed that this strategy achieves ~85%  
110 specificity, with 13-16% VIP+ in L1-4, 10% PV+ in L4-5, 15% SNCG+ in L6 (**Extended Data 2k-n**).

111 In summary, we have developed and validated two intersectional strategies to specifically target LAMP5+ cINs: one  
112 utilizing *DLX-Cre; LAMP5-FlpO* and another employing *JAM2-Cre* with a viral tool. Both strategies provide precise and  
113 reliable access to LAMP5+ cINs, predominantly located in L1 and L2/3 of the neocortex<sup>12,25</sup>. In subsequent experiments,  
114 we used both strategies concurrently, unless one offered significant advantages in terms of convenience or technical  
115 feasibility for specific experimental demands.

## 117 **LAMP5+ cIN Silencing Increased the Spontaneous Activity of PYN<sup>L23</sup> in V1**

118 The majority of LAMP5+ cINs are neurogliaform cells, whose activation results in broad and long-lasting inhibition *ex vivo*  
119 via 'volume transmission'<sup>12,18,20,21,36</sup>. Nevertheless, the *in vivo* functional contribution of this unique form of synaptic  
120 transmission from neurogliaform cells remains unclear.

121 To investigate the overall role of inhibition provided by LAMP5+ cINs within cortical circuits, we specifically blocked the  
122 synaptic transmission from LAMP5+ cINs by crossing the *DLX-Cre; LAMP5-FlpO* with the tetanus toxin effector  
123 *RC:PFto<sup>x37</sup>* (hereafter referred to as *LAMP5::TOX*) (**Figure 2a**). We then preferentially delivered GCaMP into L2/3  
124 pyramidal neurons (PYN<sup>L23</sup>) by injecting AAV9.CaMKII.GCaMP6f.WPRE.SV40 into the V1 (**Figure 2a,b**). We conducted  
125 two-photon calcium imaging to record the spontaneous activity of PYN<sup>L23</sup> in V1 of awake, head-fixed, free-running mice,  
126 which were viewing a gray screen (**Figure 2a,b**). As a control, we utilized Cre-negative and/or FlpO-negative mice  
127 (*LAMP5::CTR*) (**Figure 2a**). Silencing LAMP5+ cINs resulted in increased spontaneous activity of PYN<sup>L23</sup> (**Figure 2c**).  
128 When cross-correlating the spontaneous activity among PYN<sup>L23</sup> (**Figure 2d**), we found an increase in both the ratio of  
129 significantly correlated neuronal pairs (**Figure 2e**) and the correlation level between neuronal pairs in *LAMP5::TOX*  
130 compared with *LAMP5::CTR* (**Figure 2f, Extended Data 3a**). When we analyzed the activity of PYN<sup>L23</sup> during different  
131 behavioral states (stationary or run), we observed a higher mean activity in *LAMP5::TOX* compared to *LAMP5::CTR* only  
132 when the mice were running (**Extended Data 3b**). As a result, the difference in spontaneous activity of PYN<sup>L23</sup> between  
133 the running and the stationary state was significantly higher in *LAMP5::TOX* (**Figure 2h**).

134 VIP+ cINs are most prevalent in L2/3 and their spontaneous activities are highly correlated with locomotion speed<sup>38</sup>.  
135 However, unlike the results with LAMP5+ cIN silencing, VIP+ cIN silencing (**Extended Data 3c-e**) did not affect the highly  
136 desynchronized property of PYN<sup>L23</sup> activity (**Extended Data 3f-i**). We also did not observe any significant changes in the  
137 spontaneous activity of PYN<sup>L23</sup> during different behavioral states with VIP+ cIN silencing (**Extended Data 3j-l**).

138 Collectively, these findings suggest that LAMP5+ cINs play a critical role in desynchronizing and maintaining sparse  
139 spontaneous activity of PYN<sup>L23</sup> in V1, particularly during active behavioral state.

## 141 **LAMP5+ cIN Silencing Results in Impaired Visual Response of PYN<sup>L23</sup> in V1**

142 To explore the potential impact of the increased spontaneous activity in *LAMP5::TOX* on the visual response properties of  
143 PYN<sup>L23</sup> in V1, we exposed the mice to full-field visual stimuli consisting of moving gratings at 12 different orientations (0°  
144 to 330°, in 30° increments), while simultaneously recording the activity of PYN<sup>L23</sup> in V1 (**Figure 3a,b**). Interestingly, while

145 the ratio of responsive neurons remained unchanged (**Extended Data 4a**), we found that the average peak response at  
146 the preferred orientation was diminished in *LAMP5::TOX* compared to *LAMP5::CTR* (**Figure 3c,d, Extended Data 4b**).  
147 Given the visual responses were calculated by subtracting the baseline activity from the mean activity during visual  
148 stimulus, this reduction could be due to the elevated baseline activity in *LAMP5::TOX*, which was significantly higher  
149 (**Extended Data 4c**). Furthermore, the activity during the visual stimulus period was also reduced in *LAMP5::TOX*  
150 (**Extended Data 4c**). These findings suggest that both the elevated baseline and reduced stimulus period activities  
151 contributed to the diminished visual responses in *LAMP5::TOX*.

152 Consequently, visual responses in PYN<sup>L23</sup> of *LAMP5::TOX* exhibited a decreased SNR compared to *LAMP5::CTR* (**Figure**  
153 **3e**). In addition, *LAMP5::TOX* showed a decrease in the global orientation selectivity index (gOSI) (**Figure 3f**), suggesting  
154 a broader visual tuning curve in PYN<sup>L23</sup> in *LAMP5::TOX*. No significant changes were found in signal correlation  
155 (**Extended Data 4d**), noise correlation (**Extended Data 4e**) or the distribution of preferred orientation (**Extended Data 4f**).  
156 We observed a tendency toward an increase in the direction selective index (DSI) in *LAMP5::TOX* (**Extended Data 4g**).

157 Thus, when LAMP5+ cINs are silenced, visual responses in PYN<sup>L23</sup> exhibit reduced sharpness in orientation tuning and  
158 decreased SNR. These results suggest that LAMP5+ cINs play a pivotal role in maintaining PYN<sup>L23</sup>'s sensitivity to visual  
159 stimuli in V1.

## 161 Spontaneous Activity of LAMP5+ cINs Correlates with Behavioral States

162 Silencing LAMP5+ cINs led to increased spontaneous activity in PYN<sup>L23</sup> during locomotion (**Figure 2**), suggesting that  
163 these cINs may be recruited during active behavioral states. To understand how LAMP5+ cINs are engaged in different  
164 behavioral states, we performed *in vivo* two-photon calcium imaging and recorded the spontaneous activity of these cINs  
165 in V1 of awake behaving mice, while presenting them with a gray screen (**Figure 4a**). The activity of LAMP5<sup>L23</sup> and  
166 LAMP5<sup>L1</sup>, where most of these cINs reside, were monitored via GCaMP7s, which was specifically expressed in these cINs  
167 using the *DLX-Cre; LAMP5-FlpO; Ai195* mouse model (**Figure 4b,c**).

168 Notably, both LAMP5<sup>L23</sup> and LAMP5<sup>L1</sup> showed significantly increased spontaneous activities while the mice were running  
169 (**Figure 4d-f**). We then investigated the temporal relationship between the neural activity of LAMP5+ cINs and locomotion  
170 speed of the mice by performing the zero-time cross-correlation analysis. We found that the spontaneous activity of both  
171 LAMP5<sup>L23</sup> and LAMP5<sup>L1</sup> were highly correlated with the locomotion speed (**Figure 4g-i**). Together, these results  
172 suggested that LAMP5+ cINs were recruited during active behavioral states.



173 Moreover, a close comparison between the spontaneous activity of LAMP5<sup>L23</sup> and LAMP5<sup>L1</sup> revealed that the activity of  
174 LAMP5<sup>L1</sup> exhibited greater heterogeneity. While nearly all LAMP5<sup>L23</sup> showed increased activity during running compared  
175 to the stationary period, only 80% of LAMP5<sup>L1</sup> exhibited a similar increase (**Figure 4f**). Additionally, the zero-time cross-  
176 correlation analysis between neuronal activity and locomotion speed showed that LAMP5<sup>L23</sup> exhibited a higher ratio of  
177 neurons that had significant correlation ( $p < 0.05$  in the shuffle test, **Figure 4k**) and higher Pearson's correlation  
178 coefficients (same as the correlation value at zero-time, **Figure 4l**), indicating a stronger correlation between LAMP5<sup>L23</sup>  
179 activity and locomotion speed. These results suggested that although both LAMP5<sup>L23</sup> and LAMP5<sup>L1</sup> activities are highly  
180 correlated with locomotion speed, LAMP5<sup>L23</sup> activity were more homogenous and better correlated with locomotion in  
181 time.

182 We also examined the synchronization of activity among LAMP5+ cINs (**Extended Data 5a,b**), and found that the  
183 neuronal pairs in LAMP5<sup>L23</sup> exhibited a higher ratio of significant synchronization (**Extended Data 5c**) and higher  
184 Pearson's correlation coefficients (**Extended Data 5d**), compared to LAMP5<sup>L1</sup>. Most pairs in LAMP5<sup>L23</sup> showed positive  
185 correlation, while a small percentage of LAMP5<sup>L1</sup> pairs exhibited negative correlation within the population (**Extended**  
186 **Data 5b**). Together, these results suggested that LAMP5+ cINs may exhibit some degree of lateral inhibition within L1,  
187 which is less prevalent in L2/3<sup>16,31</sup>.

188 Finally, to further validate these results, we repeated these experiments with mice viewing a dark screen (**Extended Data**  
189 **5e-k**), yielding similar results. Secondly, we replicated the experiments with an alternative strategy *JAM2-Cre; VIP-FlpO;*  
190 *Ai65F(RCF-tdT)*, and injected AAV9.Dlx.DIO.jGCaMP8m into V1. We recorded spontaneous activity from JAM2+ neurons  
191 in L2/3 (JAM2<sup>L23</sup>) and L1 (JAM2<sup>L1</sup>), manually excluding off-targeted VIP+ cINs in L2/3 of *JAM2-Cre* from the analysis  
192 (**Extended Data 2m, Extended Data 6a**). The results from these experiments were consistent with those observed in  
193 *DLX-Cre; LAMP5-FlpO; Ai195* (**Extended Data 6**). Lastly, we performed parallel experiments investigating the  
194 spontaneous activity of VIP+ and SST+ cINs in relation to locomotion. Consistent with previous reports<sup>38-40</sup>, these results  
195 showed a strong correlation between VIP+ cIN activity and locomotion speed, while the activity of only a subset of SST+  
196 cINs was found to be modulated by locomotion (**Extended Data 7**).

197 In conclusion, our experiments reveal that the spontaneous activities of LAMP5+ cINs increase during locomotion,  
198 strongly correlate with locomotion speed and are highly synchronized. In conjunction with our previous findings (**Figure 2**),  
199 this suggests that LAMP5+ cINs hyperpolarize the baseline activity of PYN<sup>L23</sup> and may contribute to sparse cortical activity  
200 in L2/3, especially during active behavioral states. Furthermore, we demonstrate that LAMP5<sup>L23</sup> exhibit a higher degree of  
201 homogeneity in their responses and correlation with locomotion speed, whereas LAMP5<sup>L1</sup> show more heterogeneity. This

202 may arise from some degree of lateral inhibition within L1<sup>16,31</sup>, attributed to higher density of these neurons in L1, their  
203 elongated axonal morphology, combined with the non-selective inhibition properties of LAMP5+ cINs.

## 204 205 **Visual Responses and Their Modulation by Locomotion are Distinct in LAMP5<sup>L23</sup> and LAMP5<sup>L1</sup>**

206 Having established the important role played by LAMP5+ cINs in regulating cortical activity, we shifted our focus to  
207 understanding their recruitment in V1 *in vivo* during visual stimulation. Specifically, we aimed to investigate whether these  
208 neurons respond differently to visual stimuli based on their laminar position, and how these responses may change under  
209 different behavioral states.

210 We first tested the orientation tuning of LAMP5+ cINs by presenting *DLX-Cre; LAMP5-FlpO; Ai195* mice with full-field  
211 moving gratings of 12 different orientations (**Extended Data 8a**). Similar to other cINs, LAMP5+ cINs showed a broad  
212 orientation tuning curve, as indicated by low gOSI (**Extended Data 8b-c**). Additionally, we found that both LAMP5<sup>L23</sup> and  
213 LAMP5<sup>L1</sup> showed minor visual responses during the stationary period, while locomotion significantly increased their visual  
214 responses (**Extended Data 8d**).

215 Prior research has indicated the visual responses of cINs can be modulated by stimulus contrast. For example, SST+  
216 cINs exhibit stronger responses to high-contrast stimuli, whereas VIP+ cINs are more responsive to low-contrast visual  
217 gratings in V1, with PYN<sup>L23</sup> displaying mixed preferences<sup>41</sup> (we confirmed these results in **Figure 5b-c, Extended Data**  
218 **9a-c**). Here, we investigated how stimulus contrast influences the visual responses of LAMP5+ cINs. To this end, we  
219 conducted two-photon calcium imaging in V1 of awake *DLX-Cre; LAMP5-FlpO; Ai195* mice, and presented them with  
220 moving gratings of different contrasts and orientations in each trial. Each trial began with a 1s gray screen baseline,  
221 followed by 2s of moving gratings, with "blank" trials maintaining a gray screen (equal to 0% contrast) throughout the 3s  
222 duration (**Figure 5a**).

223 Results from these experiments showed that LAMP5<sup>L23</sup> responded similarly regardless of contrast levels (**Figure 5b-e**),  
224 while LAMP5<sup>L1</sup> showed a preference for lower contrast levels (**Figure 5b,c,f,g**). However, further analysis revealed that  
225 locomotion significantly increased LAMP5<sup>L23</sup> visual responses across all contrast levels, with their visual responses  
226 showing a preference for higher contrasts during running trials (**Figure 5h,i, Extended Data 9e**). Conversely, LAMP5<sup>L1</sup>  
227 continued to favor low-contrast gratings, with enhanced visual responses during locomotion (**Figure 5j,k, Extended Data**  
228 **9e**). Intriguingly, LAMP5<sup>L1</sup> showed positive responses during "blank" trials (**Figure 5f,j, Extended Data 9d**), a finding

warranting further investigation. To further support these findings, we confirmed these results using *JAM2-Cre*, *SST-Cre* or *VIP-Cre* with AAV9.Dlx.DIO.jGCaMP8m in V1 (**Extended Data 9f-q**).

Overall, our findings suggest that LAMP5<sup>L23</sup> exhibit significant visual responses and a preference for higher contrast visual stimulus, but only during active behavioral states. This suggests that LAMP5<sup>L23</sup> may require a combination of visual input and state-modulatory input to exhibit responsiveness to visual stimuli. Additionally, we found that LAMP5<sup>L1</sup> displayed greater responsiveness to lower contrast levels in both stationary and running states, with enhanced responses during locomotion. This property is similar to VIP<sup>L23</sup>, suggesting that LAMP5<sup>L1</sup> and VIP<sup>L23</sup> may share similar input connectivities involved in contrast modulation<sup>21,28,30,42-45</sup>.

### Layer-dependent circuit connectivity of LAMP5+ cINs

The variations in contrast modulation of visual responses between LAMP5<sup>L1</sup> and LAMP5<sup>L23</sup> raises the possibility that these neurons are activated by different combinations of circuit inputs within a specific context. We hypothesized that the location of their cell bodies and the morphology of their short dendrites might restrict them to being driven by different inputs.

To map the local inhibitory inputs from other cINs to LAMP5+ cINs, we conducted optogenetics-assisted circuit mapping with slice electrophysiology. Channelrhodopsin was specifically expressed in PV+, SST+ or VIP+ cINs using an intersectional *Ai80(CatCh-EYFP)* reporter mouse line crossed to *JAM2-Cre*; *SST-FlpO/VIP-FlpO/PV-FlpO* alleles (see Method - Mouse). LAMP5+ cINs were labeled via stereotaxic injection of AAV9.Dlx.DIO.dTomato into V1. Inhibitory postsynaptic currents (IPSCs) were recorded in LAMP5+ cINs by voltage clamp in the presence of tetrodotoxin (TTX) and 4-aminopyridine (4-AP) in postnatal (P) 38-42 mice (**Extended Data 10a**). Our findings revealed that SST+ cINs inhibit LAMP5+ cINs across all six cortical layers (**Extended Data 10b**). Additionally, we observed that PV+ cINs inhibit all LAMP5<sup>L2-6</sup> but not LAMP5<sup>L1</sup> (**Extended Data 10c**), likely because PV+ cINs lack axonal extensions into L1<sup>12</sup>. Furthermore, VIP+ cINs to LAMP5+ cINs connection was generally weak across all cortical layers (**Extended Data 10d**).

We next examined whether LAMP5<sup>L23</sup> and LAMP5<sup>L1</sup> are driven by different combinations of excitatory inputs based on their layer location. To do so, we explored the afferent connectivity of LAMP5+ cINs in V1 using retrograde monosynaptic rabies tracing. AAV helpers and the delta-G pseudorabies virus RVdG-mCherry were administered into V1 of adult *JAM2-Cre* mice, and brain tissue was subsequently processed after 13 days (**Figure 6a**). The starter cells were sampled in all layers of V1 (**Figure 6b**), although biased to different layers in each experiment (**Figure 6e**). Monosynaptic inputs to these

257 neurons were analyzed by aligning the sectioned brain tissues with the Allen CCFv3 atlas and calculating the ratio of  
258 rabies traced (mCherry+) cells found in a defined anatomical region to the total count of traced cells.

259 Our findings indicate that LAMP5+ cINs receive a wide range of both local V1 and long-range excitatory inputs. Major  
260 inputs to these cells in V1 originate from higher-order visual areas (HVAs), the contralateral V1 (cV1), the retrosplenial  
261 area (RSP), the secondary motor area (MOs)/anterior cingulate area (ACA), the primary somatosensory area (SSp), and  
262 auditory areas (AUD). Inputs from the visual thalamus, originate from the dorsal part of the lateral geniculate complex  
263 (LGd), the lateral posterior nucleus of the thalamus (LP), and the lateral dorsal nucleus of the thalamus (LD), as well as  
264 inputs from neuromodulatory areas like the basal forebrain (BF) were also identified (**Figure 6c-d**).

265 Furthermore, the starter cells within each of the three experiments exhibited biases towards L1, L2-5, or L5-6 populations  
266 (**Figure 6e**). This allowed us to compare differences in the afferents targeting LAMP5+ cINs in distinct laminae across  
267 experiments. We first examined local V1 inputs. L1-biased starter cells receive significant inputs from L5 (>50% of all local  
268 inputs, **Figure 6f**), consistent with the results from the prior study on NDNF+ L1 cINs in V1<sup>42</sup>. In contrast, when the starter  
269 cells were biased towards L2-5 or L5-6, >40% of local inputs originated in L2/3, followed by ~20% of inputs originating  
270 from either L4 or L5 (**Figure 6f**). LAMP5<sup>L1</sup> also showed differences in their long-range inputs compared to those in other  
271 cortical layers. L1-biased starter cells received a higher ratio of inputs from areas such as RSP, the temporal association  
272 area (TEa) (**Figure 6g**), the orbital area (ORB) (**Figure 6h**), and the higher-order visual thalamus - LP and LD (**Figure 6i**).  
273 These results aligned with the preferential innervation of L1 in V1 from these regions<sup>43,46,47</sup>. Notably, with L1-biased starter  
274 cells, we found a higher ratio of inputs from the midbrain (MB) dorsal raphe nucleus, which may houses 5-  
275 hydroxytryptamine (5-HT) serotonergic neurons, but a lower ratio of inputs from the basal forebrain pallidum (PAL), where  
276 cholinergic projection neurons may reside (**Figure 6j**).

277 In summary, monosynaptic tracing from LAMP5+ cINs showed that LAMP5<sup>L1</sup> and LAMP5<sup>L23</sup> receive distinct local and  
278 long-range inputs, likely contributing to their distinct visual response properties, such as the contrast preference.  
279 Specifically, we propose that LAMP5<sup>L1</sup> primarily receive top-down inputs targeting L1, along with local excitatory inputs  
280 from L5. In contrast, LAMP5<sup>L23</sup> rely less on top-down inputs but are driven more by inputs that convey bottom-up sensory  
281 signals (**Extended Data 10e**). Additionally, we identified local inhibitory inputs to LAMP5+ cINs in each layer. These  
282 findings underscore the variability in inputs to LAMP5+ cINs based on their laminar location, where their short dendrites  
283 restrict inputs to those in close proximity. Consequently, the source of inputs to LAMP5+ cINs is primarily determined by  
284 the axonal innervation that reaches their home layer. Overall, our results suggest that LAMP5+ cINs in different layers  
285 may be recruited differently in behavioral contexts, highlighting the importance of morphology and circuit connectivity in  
286 determining neuronal activity beyond transcriptomic types.

288 **DISCUSSION**

289 Neurogliaform cells, which comprise the majority of LAMP5+ cINs and are characterized in cortical circuits by their  
290 distinctive volume transmission output properties, remain the least studied type of cINs. This is largely due to the lack of  
291 genetic tools for targeting them. In this study, we introduced two genetic targeting strategies that selectively target  
292 LAMP5+ cINs (**Figure 1b, Extended Data 2a,b**), enabling us to explore their circuit and function *in vivo*. We found that  
293 silencing the output activity of LAMP5+ cINs leads to increased spontaneous activity in PYN<sup>L23</sup>, especially during active  
294 behavioral states (**Figure 2**). In addition, the spontaneous activity of LAMP5+ cINs was found to be highly correlated with  
295 the active behavioral states (**Figure 4**). These findings suggest that LAMP5+ cINs are likely involved in regulating the  
296 behavioral state-dependent baseline activity of PYN<sup>L23</sup>. Notably, LAMP5+ cINs in L1 versus L2/3 are differentially  
297 recruited during visual stimulation. We demonstrated that the input connectivity of LAMP5+ cINs is constrained by their  
298 specific laminar locations and short dendritic morphology (**Figure 6, Extended Data 10e**), likely contributing to the  
299 observed layer-specific preferences in contrast modulation of visual responses (**Figure 5**). Given their non-selective  
300 output properties and layer-restricted axonal arborizations, these differences in recruitment may play a crucial role in  
301 modulating distinct compartments of PYNs under different contextual conditions (**Extended Data 10f**).

302 Using our genetic labeling strategy, we observed that LAMP5+ cINs are primarily distributed in L1-3, with fewer cells in L4  
303 and L6, with the low densities being observed in L5. This observation is interesting, considering that spontaneous and  
304 evoked cortical activity tends to be sparse in L2/3 but dense in L5 within sensory cortical areas, which matches the layer  
305 distribution of LAMP5+ cINs in L2-5. It is believed that the sparsity of PYN activity in superficial layers enhances the  
306 robustness and reliability of sensory encoding, thereby improving perception<sup>48-52</sup>. Our findings, that silencing LAMP5+  
307 cINs results in increased spontaneous activity and synchrony in PYN<sup>L23</sup>, indicate that LAMP5+ cINs can be one of the key  
308 players that contribute to the observed sparsity of cortical activity in supragranular layers.

309 Although LAMP5+ cINs exhibit a continuum in their transcriptomic profiles and electrophysiological properties within the  
310 cardinal type population<sup>12,53</sup>, we believe that their layer-dependent input connectivity is crucial for shaping discrete activity  
311 patterns for LAMP5+ cINs in different cortical layers. For example, we showed that LAMP5<sup>L1</sup> predominantly responds to  
312 low-contrast visual stimuli, similar to VIP+ cINs<sup>41</sup>, while LAMP5<sup>L23</sup> preferentially responds to higher-contrast stimuli during  
313 locomotion states. This functional distinction likely results from the different combinations of inputs activating LAMP5<sup>L1</sup> or  
314 LAMP5<sup>L23</sup> during visual stimuli in different behavioral states. Brain-wide monosynaptic input analysis suggests that  
315 LAMP5+ cINs receive different inputs depending on their layer locations, primarily due to the limited reach of their short

dendrites, confining them to receive inputs from nearby axons around their cell body locations. These input differences likely explain the distinct engagement of LAMP5<sup>L23</sup> and LAMP5<sup>L1</sup> in response to various visual stimuli. For example, fewer local excitatory inputs, more long-range cortical feedback inputs, and local inhibitory inputs from SST+ cINs may collectively contribute to the similar preference for low-contrast stimuli observed in LAMP5<sup>L1</sup> and VIP+ cINs. In contrast, inputs that convey the bottom-up sensory signals, together with neuromodulatory signals in active behavioral states may drive the high contrast-preferring visual activity of LAMP5<sup>L23</sup> during locomotion (**Extended Data 10e**).

With regards to their outputs, LAMP5+ cINs also exhibit highly ramified thin axons primarily confined to their cell body layer and adjacent layers<sup>12</sup>. Although both use slow and prolonged 'volume transmission' of GABA to mediate inhibition, LAMP5<sup>L1</sup> and LAMP5<sup>L2-6</sup> may regulate cortical activity differently due to their distinct organization within the cortex (**Extended Data 10f**)<sup>22</sup>. LAMP5<sup>L1</sup>, by modulating the distal dendrites of all PYNs in L1, can modulate the activity of an entire cortical column<sup>30,54</sup>. In contrast, LAMP5<sup>L23</sup> are positioned adjacent to the somatic regions of PYN<sup>L23</sup>, and can mediate laminar-specific regulation of activity within L2/3 more directly. Furthermore, the elongated morphology of LAMP5<sup>L1</sup> and their denser distribution in L1 may contribute to lateral inhibition among LAMP5<sup>L1</sup>, resulting in the inhibition of a subset of LAMP5<sup>L1</sup> during locomotion in our spontaneous activity recordings. In contrast, LAMP5<sup>L23</sup> are likely organized in a manner that minimizes interference among themselves, illustrating the morphological adaptation of cINs in different layers to regulate layer-dependent circuit activities. Despite these differences, most LAMP5+ cINs can inhibit all other cINs within their axonal target range or couple the membrane potentials of those they are electrically gap-junctioned. This includes not only other LAMP5+ cINs but also various other cIN types<sup>22-24</sup>. These two competing aspects of LAMP5+ cINs likely contribute to the complexity of inhibitory network dynamics.

Taking into account their layer-dependent recruitment and the morphological constraints on their outputs, we believe that LAMP5<sup>L23</sup> and LAMP5<sup>L1</sup> can be engaged in different behavioral contexts, each shaping cortical activity in L2/3 in distinct ways. For example, LAMP5<sup>L23</sup> integrate a variety of inputs to monitor the local excitation levels in L2/3, while LAMP5<sup>L1</sup> may play a more active role in regulating dendritic excitation in L1 in response to higher-order feedback inputs.

Consequently, the recruitment of LAMP5<sup>L23</sup> versus LAMP5<sup>L1</sup> may not simply reflect a layer-based segregation of function but also represent an adaptive strategy to optimize cortical processing and output in response to dynamic environmental cues.

Our findings, along with those of others, have indicated that both LAMP5+ cINs and VIP+ cINs exhibit spontaneous activity highly correlated with locomotion speed in awake, behaving mice<sup>38,39</sup>. This observation is particularly interesting given the distinct inhibitory mechanisms of these two cIN populations. While LAMP5+ cINs are capable of broadly inhibiting both excitatory and inhibitory neurons, VIP+ cINs primarily function through disinhibition of PYNs on their distal

346 dendrites by inhibiting SST+ cINs<sup>55,56</sup>. These results indicate that the state-dependent modulation of cortical activity is a  
347 consequence of intricate cortical network dynamics. Notably, LAMP5+ cINs exhibit high expression levels of excitatory  
348 receptors such as adrenergic receptors (ADRA1A, ADRA1B), muscarinic cholinergic receptor (CHRM1), and nicotinic  
349 cholinergic receptors (CHRNA4, CHRNA7, CHRNB2). These receptor expressions may contribute to the observed state-  
350 dependent activity in LAMP5+ cINs, and may mediate their responsiveness to neuromodulatory signals<sup>10,27,38,57</sup>.

351 In this study, we did not distinguish the ~20% LAMP5<sup>L1</sup> that are CHRNA7+. These neurons are transcriptomically  
352 distinguishable from the rest of the LAMP5+ cINs belonging to neurogliaform cells, and they do not share similar  
353 properties as neurogliaform cells discussed above. Their axons can extend into deep cortical layers<sup>16</sup>. The circuit  
354 connectivity and function of these neurons remain unclear. While we found that the activity pattern in LAMP5<sup>L1</sup> is more  
355 heterogeneous than that seen in LAMP5<sup>L23</sup>, this is unlikely to be due to CHRNA7+ LAMP5<sup>L1</sup>, as these neurons have been  
356 reported to be more active during running state. Instead this heterogeneity is more likely to be a result of the lateral  
357 inhibition of neurogliaform cells in L1<sup>16,31,53</sup>.

358 The unique inhibition from LAMP5+ cINs may have important clinical implications. Interestingly, we found that LAMP5+  
359 cINs, particularly neurogliaform cells, exhibit the highest level of GAD2 (glutamic acid decarboxylase 65-kd isoform)  
360 expression not only in mice but also in humans<sup>27</sup>. GAD2 is primarily present in presynaptic terminals and plays a crucial  
361 role in GABA synthesis for vesicle release<sup>58</sup>. Remarkably, dysregulation of GAD2 has been implicated in neurological  
362 disorders such as epilepsy. Studies have shown that both GAD1 (glutamic acid decarboxylase 67-kd isoform) and GAD2  
363 expression levels in LAMP5+ cINs are reduced in patients with temporal lobe epilepsy<sup>26</sup>, suggesting a potential role of  
364 LAMP5+ cIN dysregulation in hypoinhibition underlying epileptogenesis. Furthermore, LAMP5+ cINs in these patients also  
365 exhibit decreased levels of SV2C (synaptic vesicle glycoprotein 2C)<sup>59</sup>, a conserved marker gene for neurogliaform cells  
366 within LAMP5+ cINs. This observation suggests that SV2C may play crucial roles in regulating vesicles in neurogliaform  
367 cells<sup>60-62</sup>.

368 In conclusion, our results highlight the functional uniqueness of LAMP5+ cINs and underscore their importance as a key  
369 population within the cortical inhibitory network. Furthermore, we advocate for the consideration of both transcriptomic cell  
370 types and circuit connectivity in parallel when categorizing cell type diversity in cortical circuits. Integrating these factors  
371 can provide a more comprehensive understanding of the functional roles of different cell populations and their  
372 contributions to cortical information processing.

373  
374

## 375 METHODS

### 376 Mouse

377 All experimental procedures were approved by and in accordance with Harvard Medical School Institutional Animal Care  
378 and Use Committee (IACUC) protocol number IS00001269. Animals were group housed and maintained under standard,  
379 temperature-controlled laboratory conditions. Mice were kept on a 12:12 light/dark cycle and received water and food ad  
380 libitum. Mice used in the *in vivo* imaging experiments were kept on a reversed light cycle. Both female and male animals  
381 were used indiscriminately for all experiments. Though a systematic analysis was not performed to assess whether there  
382 are sex-related differences, no obvious pattern was observed. Data collection and analysis were not performed blind to  
383 the conditions of the experiments. Mouse lines used in this study: *DLX-Cre* (RRID:IMSR\_JAX:008199), *LAMP5-FlpO*  
384 (RRID:IMSR\_JAX:037340, a gift from Dr. John Ngai and Dr. David A. Stafford, University of California, Berkeley),  
385 *Ai65(RCFL-tdT)* (RRID:IMSR\_JAX:021875, the Jackson Laboratory), *JAM2-Cre* (RRID:IMSR\_JAX:031612, the Jackson  
386 Laboratory), *Ai65F(RCF-tdT)* (RRID:IMSR\_JAX:032864, the Jackson Laboratory), *RC:PFTox*<sup>37</sup> (a gift from Dr. Susan  
387 Dymecki and Dr. David Ginty, Harvard Medical School), *Ai195* (RRID:IMSR\_JAX:034112, a gift from Dr. Tanya L. Daigle,  
388 Dr. Bosiljka Tasic and Dr. Hongkui Zeng, Allen Brain Institute), *VIP-FlpO* (RRID:IMSR\_JAX:028578, the Jackson  
389 Laboratory), *SST-FlpO* (RRID:IMSR\_JAX:031629, the Jackson Laboratory), *PV-FlpO* (RRID:IMSR\_JAX:022730, the  
390 Jackson Laboratory). All mice were maintained in house on a C57BL/6J (RRID:IMSR\_JAX:000664, the Jackson  
391 Laboratory) background.

392 Genetic strategy with *JAM2-Cre*: We chose *JAM2-Cre* because *JAM2* is a conserved marker gene for neurogliaform cells  
393 (**Extended Data 1a1**). However, *JAM2* is also expressed in germ cells, with its expression becoming restricted to  
394 LAMP5+ cINs only in adults. This limits the use of this strategy to adult ages. In our experiments, *JAM2-Cre* served not  
395 only as a targeting tool for LAMP5+ cINs in adults using AAV, but also as a *Germline-Cre* to convert intersectional mouse  
396 lines (*RC:PFTox*, *Ai195*, or *Ai80*) into Flp-dependent mouse lines. Through DNA genotyping, we observed that offspring  
397 bred from *JAM2-Cre* mice and intersectional reporters became a Flp-dependent reporter. We found that *JAM2* RNA has  
398 been detected in germ cells, including sperm<sup>63,64</sup>, suggesting that Cre activity in *JAM2-Cre* mice is activated in germ cells.  
399 Therefore, *JAM2-Cre* was also used as a *Germline-Cre* in our experiments.

### 400 Plasmid construction

401 pAAV.Dlx.DIO.jGcamp8m plasmid was constructed by first flipping the MCS with BclI with the backbone pAAV-VTKD2  
402 (Addgene #170847)<sup>65</sup>, then inserting the jGCaMP8m<sup>66</sup> fragment from pGP-AAV-syn-jGCaMP8m-WPRE (Addgene  
403 #162375) digested by EcoRI and HindIII. pAAV.Dlx.DIO.dTom has been donated to Addgene (Plasmid #83894)



404 previously<sup>34</sup>. pAAV.Dlx.DIO.TVA was constructed by inserting the hDlx promoter fragment from pAAV-VTKD2 (Addgene  
405 #170847) into the backbone pAAV-EF1a-flex-TVA (Addgene #69618), digested by EcoRI and HindIII.  
406 pAAV.Dlx.DIO.GFP.N2cG was constructed by Gibson assembly the PCR fragment GFP-P2A-N2cG from pAAV-VTKS2-  
407 TVA-eGFP-N2cG (Addgene #175439) into the backbone pAAV-VTKD2 (Addgene #170847)<sup>65</sup> digested by EcoRI and  
408 HindIII.

#### 409 Cell culture, transfection and AAV production

410 HEK293FT cells (Thermo Fisher Scientific, #R70007) were cultured in Dulbecco's Modified Eagle's medium with high  
411 glucose and pyruvate, GlutaMAX Supplement, 10% fetal bovine serum, penicillin (100 units/ml) and streptomycin (100  
412 µg/ml). The cultures were incubated at 37 °C in a humidified atmosphere containing 5% CO<sub>2</sub>. For AAV production,  
413 HEK293FT cells were seeded on 15-cm dishes without antibiotics for close to 24 hours and co-transfected with the  
414 following plasmids using Polyethylenimine (100 µg/dish, Polysciences, #23966-1): pHGTI-Adeno1 helper (22 µg/dish),  
415 AAV9 helper (Addgene plasmid #112865, 9 µg/dish), and the AAV expression vector (12 µg/dish). 72 hours after  
416 transfection, transfected cells were harvested and lysed (150 mM NaCl, 20 mM Tris pH 8.0) by three freeze-thaw cycles  
417 and Benzonase treatment (375 U/dish; Sigma, #E1014) for 30 min at 37 °C. The supernatants were cleared by  
418 centrifugation at 4000 RPM for 20 min at 25 °C, then transferred to Iodixanol gradients (OptiPrep Density Gradient  
419 Medium, Sigma, #D1556) for ultracentrifugation (VTi50 rotor, Beckman Coulter) at 50,000 RPM for 1.5 hr at 16 °C. The  
420 40% iodixanol fraction containing the AAVs was collected, underwent ultrafiltration with PBS in Amicon Ultra-15  
421 Centrifugal Filter (15 ml, 100kDa MWCO, Millipore, #UFC910024) at 4000 RPM for 1 hr for 4 times, aliquoted and stored  
422 at -80 °C. The number of genomic viral copies was determined by qPCR using the following primers against the WPRE  
423 sequence: Fw: AGCTCCTTTCCGGGACTTTC and Rv: CACCACGGAATTGTCAGTGC.

#### 424 *In vivo* imaging: cranial window and virus injection surgery

425 For in vivo imaging experiments, surgeries were carried out in mice after they were 2 months old. 1 Rimadyl (2 mg/tablet,  
426 Bio-serv, #MD150-2) tablet per animal was placed in the cage 1 day prior to the surgery. Mice were anesthetized with  
427 isoflurane (5% for induction, 1-2% during surgery, in O<sub>2</sub>), mounted in a stereotaxic frame, and kept on a warm blanket  
428 (34 °C). The eyes were moistened with lubricant eye ointment (Systane). The scalp was disinfected with 10% Povidone-  
429 Iodine (PDI, #S41125) and a section of scalp was removed using microscissors. 0.3% hydrogen peroxide was applied on  
430 the skull to oxidize and facilitate removal of periosteal tissue with cotton tip swabs, and washed with sterile saline. The 3  
431 mm cranial window was centered around 2.5 mm lateral to the midline (left hemisphere) and 1.5 mm anterior to the  
432 transverse sinus (or Lambda suture), skull was removed with 3 mm biopsy punch (Integra™ 3332) and micro knives (Fine

433 Science Tools, 10315-12). Virus injections in V1 were performed using beveled glass micropipettes (Drummond, 3-000-  
434 203-G/X) with Nanoject III (Drummond). 300 nl of virus was injected into each of the 2-3 locations, at 3 depths (0.43, 0.38  
435 and 0.33 mm) below the dura. AAV2/9.CaMKII.GCaMP6f.WPRE.SV40 was diluted to 6.7E+12 vector genomes per ml  
436 (vg/ml) with 1X PBS prior to injection for Tox experiments. AAV2/9.VTKD2.jGcamp8m was diluted to 1.0E+13 vg/ml with  
437 1X PBS prior to injection to *JAM2<sup>Cre</sup>* mice. No virus injections were performed in the GCaMP reporter (Ai195) mice. The  
438 cranial window was kept moist with sterile saline during virus injection and sealed with two circular, pre-sanitized glass  
439 coverslips, 3 mm and 5 mm in diameter (Warner Instruments, #64-0700 and #64-0720), individually conjoined with optical  
440 adhesive (Norland, NOA 71). The 3 mm coverslip was laid over the pia surface within the cranial window. Tissue adhesive  
441 (3M Vetbond) was applied around the 3 mm coverslip. A custom-designed head plate was adhered over the glass window  
442 with Super Glue gel (Loctite) and C&B Metabond (Parkell, #171032) mixed with black powder paint. Mice were given  
443 Buprenorphine SR 0.5-1.0 mg/kg SC after the surgery and monitored for 5 days post-surgery.

#### 444 *In vivo* imaging: intrinsic imaging

445 Intrinsic optical signal imaging was conducted via the cranial window of head-fixed mice. Prior to imaging, mice received  
446 an intramuscular injection of 0.2mg/ml chlorprothixene (Sigma-Aldrich, Y0002088) at a dosage of 80µl per 20g of body  
447 weight, administered at least 15 minutes before the experiment. During imaging, additional 0.5-0.75% isoflurane  
448 anesthesia (in O<sup>2</sup>) was applied to mice, and the heat pad (34°C) was used to maintain body temperature. Illumination of  
449 the cortex was achieved using a white LED cold light source equipped with light guides and a filter slider (Leica, KL1600).  
450 For vessel imaging, a green filter (Schott, 258.304) was inserted, while intrinsic signals were recorded under a red filter  
451 (Schott, 258.303). Tandem lens systems were used, consisting of a Nikkor 85mm F2.0 AI-S (Nikon) as the top lens and  
452 an AF Nikkor 50mm f/1.8D (Nikon) as the bottom lens. Additionally, green (Edmund, #87-801) and red (Edmund, #88-018)  
453 emission filters were optionally used during vessel imaging and intrinsic signal recording, respectively, although they were  
454 not essential. Data acquisition was performed using a USB camera (FLIR, BFS-U3-19S4M-C)<sup>67</sup> and SpinView 2.5.0.80  
455 software. The image format for acquisition was configured to 12 bits, with a binning setting of 2 x 2 pixels, resulting in  
456 recordings at a resolution of 808 x 620 pixels with a pixel size 5.3 x 5.3µm. Vessel images were captured at the beginning  
457 of the experiment, then the lenses were focused around 0.5mm below the surface. Visual stimuli were generated using  
458 custom MATLAB (Mathworks) scripts with Psychtoolbox-3<sup>68,69</sup> and presented at a distance of 16 cm from the right eye on  
459 a gamma-corrected LED-backlit LCD monitor (Dell P2317H, 509mm X 286mm) with a mean luminance of 20 cd/m<sup>2</sup>. Each  
460 trial consisted of a 2s baseline period (full screen RGB black), followed by 1s of visual stimulation and 20s post-stimulus  
461 interval for recovery (full screen RGB black). The visual stimulation comprised four-direction full-field drifting gratings (at  
462 0°, 45°, 90°, and 135°, each lasting 250ms) with 100% contrast, a temporal frequency of 2Hz, and a spatial frequency of

0.04 cycles per degree (cpd)<sup>70</sup>. A total of 20-25 trials were repeated, with a frame rate set at 58.89Hz, and 1000 frames were recorded for each repetition. A small block of bright pixels was positioned at the bottom left corner of the screen at the beginning of each trial. This signal was captured by a photodiode (Thorlabs, SM05PD1A) affixed to a duplicate secondary screen, processed by a custom current-to-voltage converter to generate a trigger for initiating the recording. V1 activation was identified by averaging frames across repetitions, obtaining the mean during the 2s baseline and during the 0.5s post-stimulus period, and then calculating the ratio of the post-stimulus mean to the baseline mean, where significant intrinsic signals were detected. These signals were then superimposed onto the vessel images to locate V1 for subsequent two-photon imaging.

*In vivo* imaging: data acquisition and preprocessing

#### *Locomotion speed*

Following a two-week post-surgical recovery period, mice were habituated to head fixation for a minimum of 5 days until they demonstrated free running on the custom-built cylindrical treadmill (made in-house using an 8(W) x 4(H) inch round foam cake dummy and a rod through the center, surface covered with black Gaffers tape) before imaging experiments started. A E2 encoder (US Digital) was used to read out the shaft speed and the obtained digital signal was then converted into an analog voltage using a microcontroller (Arduino Micro) and was sent to NI DAQ for acquiring locomotion speed data at 30kHz using Thorsync 4.0 (Thorlabs). Speed data was smoothed with 1D convolution, binned to 30 Hz, and converted to cm/s unit using custom MATLAB and Python scripts.

#### *Pupillometry*

An in-house-built pupillometry system was used to monitor eyelid blinks and pupil changes. An infrared (850nm) LED (CM-IR30, CMVision) was used to illuminate the left eye (ipsilateral to the recording site). To evenly diffuse the light, an opaque piece of plastic was placed in front of the LED. Video recording was conducted with 1280 x 1024 pixels, at a frame rate of 19.06 Hz using a Chameleon3 monochrome camera (PointGrey FLIR, CM3-U3-13Y3M-CS) and the PointGrey FlyCap2 2.13.3.61 software. The Chameleon3 camera was equipped with a lens (Thorlabs, MVL16M23) attached via an extension adapter (Thorlabs, CML05). To minimize interference from ambient light and the two-photon laser, a 850/40 nm bandpass filter (Thorlabs, FB850-40) was positioned in front of the camera lens. Video preprocessing was performed offline using Fiji<sup>71</sup> and Facemap<sup>72</sup>, followed by further processing with custom Python scripts. Frames containing artifacts from the trigger signal were removed at the start of the recording. Both blink and pupil data were z-scored for normalization. The blink data was smoothed with a Hanning window, and velocity calculation was performed to detect blink onset and offset. Blinks were adjusted by adding a buffer period before onset and after offset, with nearby

492 blinks merged if a predefined threshold was met. Frames containing blinks were excluded from pupil data, and the  
493 resulting gaps were filled using cubic spline interpolation<sup>73</sup>.

#### 494 *Visual stimuli and trial design*

495 Visual stimuli were generated using custom MATLAB (Mathworks) scripts with Psychtoolbox-3<sup>68,69</sup> and presented at a  
496 distance of 16 cm from the right eye on a gamma-corrected LED-backlit LCD monitor (Dell P2317H, 509mm X 286 mm)  
497 with a mean luminance of 20 cd/m<sup>2</sup>.

498 In the spontaneous activity experiments, the screen was set to either a powered off state (dark screen experiment) or  
499 displayed a uniform mean luminance (gray screen experiment), the recordings usually last 730s.

500 In the visual orientation tuning experiments, a 10s gray screen preceded the trials as the baseline. Each 6s trial,  
501 randomized in order, began with a 1s gray screen, followed by 2s of full-screen moving gratings at 80% contrast, with a 1  
502 Hz temporal frequency and a 0.04 cpd spatial frequency, and ended with a 3s gray screen. The moving gratings were  
503 presented in 12 distinct orientations, each separated by 30 degrees and were repeated 10 times for interneuron imaging  
504 or 30 times for excitatory neurons in the Tox experiments.

505 In the visual contrast tuning experiments, a 10s gray screen preceded the trials as the baseline. Each 3s trial began with a  
506 0.8s gray screen, followed by 2s of full-screen moving gratings at one of six contrasts (80%, 60%, 40%, 20%, 10%, 5%),  
507 one of eight orientations (45 degrees apart), with a 1Hz temporal frequency and a 0.04cpd spatial frequency, and ended  
508 with a 0.2s gray screen. Each condition was repeated 15 times, with one blank trial randomly placed in (a continued gray  
509 screen instead of moving gratings) every 20 trials. All trials were randomized in order.

#### 510 *Two-photon calcium imaging*

511 Imaging was performed with a custom-built two-photon microscope (Thorlabs, Bergamo®) equipped with a 8 kHz galvo-  
512 resonant scanner, Pockels cells and photomultiplier modules (PMTs). Tunable ultrafast lasers (Spectra-Physics,  
513 InSight®X3) were set at 920nm (tunable) for GCaMPs and 1045nm (fixed) for tdTomato. The objective was a 16x water  
514 immersion lens with a 0.8 numerical aperture (Nikon). Images were acquired with a 512 × 512 pixels field of view (412 x  
515 412µm), targeting cells in L1 (<100µm under the pia mater) or L2/3 (120–250µm under the pia mater), using ThorImage  
516 4.3 (Thorlabs) at a frame rate of 30 Hz. The laser power was adjusted up to 50 mW at the objective's front aperture.

517 During the imaging, the ultrasound water gel was used under the objective and black masking tape (Thorlabs, T743-1.0)  
518 was used to shield light from the screen.

519 To synchronize calcium imaging, locomotion speed, and pupillometry recordings, a small block of bright pixels was  
520 positioned at the bottom left corner of the screen. This signal was captured by a photodiode (Thorlabs, SM05PD1A)

521 affixed to a duplicate secondary screen, processed by a custom current-to-voltage converter to generate a trigger,  
522 ensuring precise synchronization across the different data streams.

523 Calcium imaging data were preprocessed with Suite2p<sup>74</sup> for motion correction and region of interest (ROI, or neuron)  
524 extraction. Sessions with significant z-drift movement were excluded. In some experiments, tdTomato signals were  
525 recorded as control for movement, and no significant signals were observed during locomotion of the animals. For every  
526 recorded field of view, detected ROIs were semi-manually adjusted based on identifiable cell bodies. ROIs with lower  
527 somatic than neuropil signals were excluded. Raw traces extracted by Suite2p were further processed in Python with  
528 custom scripts. Neuropil contamination was corrected using  $F = F_{somatic} - F_{neuropil} * neuropil\ factor\ (r)$  with  $r =$   
529  $0.7$  for GCaMP6f<sup>75</sup> and GCaMP7s<sup>76</sup>, and  $r = 0.8$  for jGCaMP8m<sup>66,77</sup>. Baseline fluorescence (F0) was estimated by  
530 identifying the 30th percentile over a moving window of 150s<sup>41</sup>. dF/F0 traces were computed by subtracting and dividing  
531 the raw trace by F0. To get standardized dF/F0, dF/F0 traces were then normalized by subtracting the median and  
532 dividing by the standard deviation<sup>78</sup>.

### 533 *Data storage*

534 All preprocessed data were stored in HDF5 format using Python and experimental metadata were stored into a database  
535 with MySQL Workbench 8.0.34.

### 536 *In vivo* imaging: data analysis

#### 537 *Synchronization of activity*

538 To assess the synchronization of neuronal activity, the standardized dF/F0 for each identified ROIs (neurons) was  
539 interpolated to 10 Hz, smoothed with a 5-point moving average, and then decimated to 5 Hz. ROIs with standardized  
540  $dF/F0 \geq 3$  (at least 3-fold standard deviations from the mean) were included for this analysis. Pairwise zero-time cross-  
541 correlation, and Pearson's correlation coefficients were computed based on the 5 Hz activity data from identified ROIs  
542 within the same field of view (FOV). The significance of correlation ( $p < 0.05$ ) was computed by shuffling one of the paired  
543 activities 1000 times.

#### 544 *Spontaneous activity*

545 To evaluate the spontaneous activity of neurons, the standardized dF/F0 of each ROI (neuron) were processed, along  
546 with locomotion speed and z-scored pupil area. ROIs with standardized  $dF/F0 \geq 3$  (at least 3-fold standard deviations from  
547 the median) were included for further analysis. Experimental recordings were excluded if the mouse did not run during the  
548 trial. To assess the spontaneous activity of neurons, frames were classified based on the subject's movement status:

stationary (speed  $\leq 1$  cm/s) and running (speed  $> 1$  cm/s). The average neuronal activity during each state was computed for individual neurons. The 2D density plot was plotted with the 'scipy.stats.gaussian\_kde' function in Python. For correlation between neuronal activity and locomotion speed, data were first interpolated to a 10 Hz sampling rate, smoothed using a 5-point moving average, and then decimated to 5 Hz. The zero-time cross-correlation between neuronal activity and locomotion speed was computed, and the Pearson's correlation coefficients were calculated at zero-time. The significance of these correlations was assessed through a shuffle test involving 1000 permutations of the locomotion speed data, with a significance threshold set at  $p < 0.05$ . Neurons displaying significant correlations were further analyzed to identify the maximum correlation value and the corresponding time lag.

### *Orientation visual responses*

To investigate the orientation tuning properties of neurons in V1, their visual responses to drifting gratings were analyzed at the population level. Visual responses were calculated on the average standardized  $dF/F_0$  during the period of moving grating presentation, adjusted by subtracting a 0.5s baseline period prior to the onset of the grating for each trial, then the responses were averaged across multiple repeats for each orientation tested for individual neurons. The neuron was categorized as a responsive neuron if in at least two trials it had a response that was 3 times larger than standard deviation of the baseline.

The global orientation selectivity index (gOSI) was calculated with

$$gOSI = \left| \frac{\sum R(\theta) e^{2i\theta}}{\sum R(\theta)} \right|$$

where  $\theta$  was the orientation angle of moving gratings, and  $R(\theta)$  denoted the mean response to moving gratings at that orientation,  $i$  was the imaginary unit.

The direction selectivity index (DSI) was calculated with

$$DSI = \frac{R_{pref} - R_{null}}{R_{pref} + R_{null}}$$

where  $R_{pref}$  was the neuron's average response to the preferred orientation (the orientation that elicits the strongest response) and  $R_{null}$  was its averaged response to the antipodal orientation ( $180^\circ$  opposite to the preferred orientation). To avoid the impact of negative values in the standardized  $dF/F_0$  data, we normalize the response following  $(R - R_{min}) / (R_{max} - R_{min})$  before calculation of gOSI and DSI.

The SNR was calculated by averaging across  $SNR_\theta$  for each neuron. For each orientation, it was computed by dividing the square of the mean response by the standard deviation of responses to repetitions for each orientation.

Signal correlations were calculated for each neuronal pair from the same recording. To avoid spontaneous correlations, half of the repetitions were randomly selected from neuron  $j$  to get the mean response for each orientation. The mean

response from neuron  $k$  was averaged from the other half repetitions for each orientation. The neuron's mean response to each orientation was calculated as  $\bar{R}$ .

$$\bar{R} = [\bar{R}_0, \bar{R}_{30}, \bar{R}_{60}, \dots, \bar{R}_{330}]$$

Pairwise signal correlation  $\rho_{j,k}^{signal}$  was calculated as the Pearson's correlation coefficient between  $\bar{R}_j$  and  $\bar{R}_k$ :

$$\rho_{j,k}^{signal} = corr(\bar{R}_j, \bar{R}_k)$$

where  $j$  and  $k$  indicate neuron  $j$  and neuron  $k$ , respectively.

Noise correlations were calculated for each neuronal pair from the same recording<sup>79</sup>. The neuron's response to each repetition of that orientation  $\theta$  was denoted as:

$$R_\theta = [R_{\theta,1}, R_{\theta,2}, R_{\theta,3}, \dots, R_{\theta,n}]$$

where  $n$  is the number of repetitions per orientation. Pairwise noise correlation  $\rho_{j,k}^{noise}$  was calculated as the averaged Pearson's correlation coefficient between  $R_{j,\theta}$  and  $R_{k,\theta}$  across all 12 orientations:

$$\rho_{j,k}^{noise} = \frac{\sum_{\theta=0}^{330} corr(R_{j,\theta}, R_{k,\theta})}{12}$$

### *Contrast responses of cINs*

To access the visual responses of cINs to moving gratings of varying contrasts, visual response for each trial was calculated as the mean standardized dF/F0 activity during the presentation of moving grating stimuli subtract the mean activity from baseline (the 0.5s period before the stimuli). The neuron was considered responsive and included in the analysis if it exhibited responses in at least two trials that were more than three times the standard deviation of the baseline activity. In this experiment, almost all neurons recorded were identified as 'responsive'. Visual responses were averaged across multiple repetitions for different orientations at the same contrast level. Contrasts of 5% and 10% were classified as low contrasts, while 60% and 80% contrasts were considered high contrasts. Trials were classified into stationary (mean speed  $\leq 1$  cm/s) or running (mean speed  $> 1$  cm/s) trials based on the averaged speed during visual stimulus presentation for each trial. Contrast preference computed by the log-scale center-of-mass  $c_{COM}$ <sup>41</sup>, which was calculated from mean visual responses to various contrast stimuli averaged across all orientations:

$$c_{COM} = \exp\left(\frac{\sum R_c \ln c}{\sum R_c}\right)$$

where  $c$  is the contrast of moving gratings,  $R_c$  is the averaged visual responses across all orientations at contrast  $c$ .

603 Retrograde monosynaptic rabies tracing

604 For tracing inputs from LAMP5+ cINs in V1, JAM2<sup>Cre</sup> mice at 2-5 month-old were stereotaxically injected with  
605 AAV1.DLX.DIO.TVA (titer:  $3.5 \times 10^{12}$  vg/mL, diluted to  $9 \times 10^{11}$  vg/mL), AAV1.DLX.DIO.GFP.N2cG (titer:  $2.9 \times 10^{12}$  vg/mL,  
606 diluted to  $7 \times 10^{11}$  vg/mL) and rabies virus EnvA-pseudotyped CVS-N2c(DG)-FlpO-mCherry (titer:  $3.7 \times 10^9$  U/ml, diluted  
607 to  $1 \times 10^8$  U/ml) at the same time in V1 (from Bregma: AP -3, ML  $\pm 2.5$ , DV 0.25-0.5 mm) with a total volume of 60 nl using  
608 Nanoject III (Drummond) at 1nl/s. The rabies virus construct was a gift from Thomas Jessell (Addgene #73471<sup>80</sup>) and  
609 EnvA-pseudotyped CVS-N2c( $\Delta$ G)-FlpO-mCherry was generously shared by K. Ritola at Janelia Farms Research Center  
610 as described in <sup>81</sup>.

611 Animals were sacrificed and perfused 13 days later and brain tissue was collected. Fixed brain samples were sectioned to  
612 50  $\mu$ m slices with vibratome (Leica). Sections were analyzed every 150  $\mu$ m along the rostral-caudal axis with  
613 immunohistochemistry to examine the rabies tracing patterns. Images were collected using a whole slide scanning  
614 microscope with a 10X objective (Olympus VS120 slide scanners).

615 NeuroInfo software (MBF Bioscience) was used for image registration and cell detection. All brain sections were manually  
616 reordered from rostral to caudal of the brain and the border of each brain section was identified. Initial alignment of  
617 sections utilized the software's Most Accurate alignment option, followed by manual adjustments as necessary. A fixed  
618 distance of 150  $\mu$ m between each section was specified. The Section Registration function of the software was then used  
619 to estimate the rostral-caudal location of each section by comparing it to an Allen Mouse Brain Common Coordinate  
620 Framework. Non-linear registration was applied to account for any minor distortions introduced during sectioning,  
621 mounting, or imperfections in sectioning angle. Cell detection parameters, including cell size and distance from  
622 background, were adjusted to optimize detection accuracy. Detection of rabies-infected cells in the red channel was  
623 performed using a Neural Network with the preset pyramidal-p64-c1-v15.pbx. Detected cells were manually reviewed to  
624 correct any potential detection errors. Additionally, starter cells were manually identified and marked as GFP co-localized  
625 rabies-infected cells.

626 Perfusion

627 For all histological experiments, mice were deeply anesthetized with sodium pentobarbital (Euthasol) by intraperitoneal  
628 injection and transcardially perfused with 1X PBS followed by 4% paraformaldehyde (PFA) in 1X PBS. Brains were  
629 dissected out and post-fixed overnight at 4°C or 2 hours at room temperature. Fixed brain samples were then  
630 cryopreserved in 30% sucrose in 1X PBS.



631 Immunohistochemistry

632 40  $\mu$ m brain sections (if not specifically stated) were obtained through a Leica sliding microtome and preserved in the  
633 antifreeze buffer (30% glycerol, 30% ethylene glycol in 1X PBS) and stored at -20°C before experiments. Free-floating  
634 brain sections were incubated in blocking solution (10% normal donkey serum, 0.3% Triton X-100 in 1X PBS) at room  
635 temperature for 1 hour, followed by incubation in primary antibody diluted in blocking solution at 4°C overnight. The  
636 following day, sections were rinsed in 1X PBS for 10 minutes 3 times, followed by secondary antibody incubation in the  
637 same blocking solution for 1 hour at room temperature. Sections were then rinsed in 1X PBS for 10 minutes 3 times.  
638 Sections were counterstained with DAPI (5  $\mu$ M in 1x PBS, Sigma #D9542) for 5 minutes and mounted using Fluoromount-  
639 G (Invitrogen). Images were collected using a whole slide scanning microscope with a 10X objective (Olympus, VS120  
640 slide scanner) or using a motorized tiling scope (Zeiss, Axio Imager A1) with a 10X objective. Primary antibodies used in  
641 this study include Rabbit-anti-DsRed (Clontech #632496, 1:1000), Goat anti-GFP (Sicgen, #AB0020-200), Chicken-anti-  
642 GFP (Aves Labs, #1020), Rabbit-anti-SST (Peninsula Laboratories, #T4103, 1:3000). Secondaries (dilute at 1:500) used  
643 in this study include Alexa Fluor 488 Donkey anti-Goat (Thermo Fisher Scientific, #A-11055), Alexa Fluor 488 Donkey  
644 anti-Chicken (Jackson ImmunoResearch Labs, #703-545-155), Alexa Fluor 594 Donkey anti-Rabbit (Thermo Fisher  
645 Scientific, #A-21207), Alexa Fluor 647, Donkey anti-Rabbit (Thermo Fisher Scientific, #A-31573).

646 RNAscope<sup>®</sup> with Immunohistochemistry

647 20  $\mu$ m brain sections were obtained using a Leica sliding microtome and preserved in section storage buffer (28% (w/v)  
648 sucrose, 30% (v/v) ethylene glycol in 0.1M sodium phosphate buffer, pH 7.4) and stored at -80 °C before the RNAscope<sup>®</sup>  
649 experiments. Samples were processed according to the ACDBio Multiplex Fluorescent v2 Kit protocol (ACDBio #323100)  
650 for fixed frozen tissue. Briefly, tissue was pre-treated with a series of dehydration, H<sub>2</sub>O<sub>2</sub>, antigen retrieval, and protease  
651 III steps before incubation with the probe for 2 hours at 40 °C. Note here protease III incubation was performed at room  
652 temperature to better preserve protein. Three amplification steps were carried out prior to developing the signal with  
653 Opal<sup>™</sup> or TSA<sup>®</sup> Dyes (Akoya Biosciences). Immunostaining following the RNAscope<sup>®</sup> experiment was performed in some  
654 experiments according to Technical Note 323100-TNS from ACDBio. Primary antibody Rabbit-anti-DsRed (Clontech  
655 #632496, 1:1000) and secondary antibody HRP-goat-anti-rabbit (1:500) was used, followed by Opal<sup>™</sup> or TSA<sup>®</sup> Dyes for  
656 tdTomato or dTomato protein immunostaining. Sections were counterstained with DAPI (5  $\mu$ M, Sigma #D9542) and  
657 mounted using Fluoromount-G (Invitrogen) or Prolong Gold antifade mounting medium. Images of RNAscope<sup>®</sup>  
658 experiments were acquired with an upright confocal microscope (Zeiss LSM 800) with a 10X or 20X objective (Plan-  
659 Apochromat 10x/0.45 420640-9900, 20x/0.8 420650-9901). To analyze the marker RNA expression in genetically labeled  
660 neurons, labeled neurons were segmented using threshold method after background subtraction and applying gaussian

661 blur filter in Fiji. Probe signals were detected by thresholding methods and the presence of probe signals within the  
662 boundary of segmented neurons was quantified as probe-positive labeled neurons. Probes used in this study include:  
663 DLX5-C1(#478151), GAD2-C2(#400951-C2), LHX6-C1(#422791), LSP1-C3(#511811-C3), NPY-C2(#313321-C2), NDNF-  
664 C1(#447471), NDNF-C3(#447471-C3), PVALB-C1(#421931), SNCG-C1(#482741), SST-C1(#404631), SV2C-  
665 C1(#545001), VIP-C3(#415961-C3).

666 *In vitro* electrophysiology: whole-cell patch clamp

667 Mice were perfused with NMDG-HEPES aCSF containing 93 mM NMDG (Sigma, #M2004), 2.5 mM KCl (Sigma, #P9541),  
668 1.2 mM NaH<sub>2</sub>PO<sub>4</sub> (Himedia, #GRM3964), 30 mM NaHCO<sub>3</sub> (Sigma, #S6014), 20 mM HEPES (Sigma, #H3375), 25 mM  
669 glucose (Sigma, #G8270), 2 mM thiourea (Sigma, #T8656), 5 mM Na-ascorbate (Sigma, #A4034), 3 mM Na-pyruvate  
670 (Sigma, #P2256), 0.5 mM CaCl<sub>2</sub>·2H<sub>2</sub>O (Quality Biological, #351-130-721) and 10 mM MgSO<sub>4</sub>·7H<sub>2</sub>O (Quality Biological,  
671 #351-033-721), equilibrated with hydrochloric acid (Sigma, #H1758) to pH 7.3–7.4. Mice were then decapitated, and the  
672 brain was quickly removed and immersed in NMDG-HEPES aCSF. 300 μm thick coronal slices were cut using a  
673 vibratome (Leica VT 1200S) through V1. Slices were recovered in a holding chamber with HEPES holding aCSF  
674 containing 92 mM NaCl (Sigma, #S3014), 2.5 mM KCl (Sigma, #P9541), 1.2 mM NaH<sub>2</sub>PO<sub>4</sub> (Himedia, #GRM3964), 30 mM  
675 NaHCO<sub>3</sub> (Sigma, #S6014), 20 mM HEPES (Sigma, #H3375), 25 mM glucose (Sigma, #G8270), 2 mM thiourea (Sigma,  
676 #T8656), 5 mM Na-ascorbate (Sigma, #A4034), 3 mM Na-pyruvate (Sigma, #P2256), 2 mM CaCl<sub>2</sub>·2H<sub>2</sub>O (Quality  
677 Biological, #351-130-721) and 2 mM MgSO<sub>4</sub>·7H<sub>2</sub>O (Quality Biological, #351-033-721), equilibrated with NaOH (Macron,  
678 #7708-10) or hydrochloric acid (Sigma, #H1758) to pH 7.3–7.4. During recovery, the NaCl was gradually added as  
679 described in <sup>82</sup>. Slices were recovered at 34 °C for 25 minutes and at room temperature for at least 45 minutes prior to  
680 recording. All slice preparation and recording solutions were oxygenated with carbogen gas (95% O<sub>2</sub>, 5% CO<sub>2</sub>, pH 7.4).  
681 For recordings, slices were transferred to an upright microscope (Zeiss) with IR-DIC optics. Cells were visualized using a  
682 40x water immersion objective. Slices were perfused with HEPES recording aCSF in a recording chamber at 2 mL/min at  
683 30°C. HEPES recording aCSF contains 124 mM NaCl (Sigma, #S3014), 2.5 mM KCl (Sigma, #P9541), 1.2 mM NaH<sub>2</sub>PO<sub>4</sub>  
684 (Himedia, #GRM3964), 24 mM NaHCO<sub>3</sub> (Sigma, #S6014), 5 mM HEPES (Sigma, #H3375), 12.5 mM glucose (Sigma,  
685 #G8270), 2 mM CaCl<sub>2</sub>·2H<sub>2</sub>O (Quality Biological, #351-130-721) and 2 mM MgSO<sub>4</sub>·7H<sub>2</sub>O (Quality Biological, #351-033-  
686 721), equilibrated with NaOH (Macron, #7708-10) or hydrochloric acid (Sigma, #H1758) to pH 7.3–7.4. Patch electrodes  
687 (4–6 MΩ) were pulled from borosilicate glass (1.5 mm OD, Harvard Apparatus). For all recordings patch pipettes were  
688 filled with an internal voltage-clamp solution containing: 130 mM Cs-methanesulfonate (Sigma, #C1426), 5 mM CsCl  
689 (Sigma, #C3032), 10 mM HEPES (Sigma, #H3375), 0.2 mM EGTA.CsOH (Sigma, #E3889), 4 mM MgATP (Sigma,  
690 #A9187), 0.3 mM Na<sub>2</sub>GTP (Sigma, #G8877), 8 mM Phosphocreatine-Tris<sub>2</sub> (Sigma, #P1937), 5 mM QX314-Cl (Tocris,

691 #2313), 0.4% biocytin (Sigma, #B4261), equilibrated with 0.5 M CsOH at pH 7.3, or an internal current-clamp solution  
692 containing: 130 mM K D-gluconate (Sigma, #G4500), 5 mM KCl (Sigma, #P9541), 10 mM HEPES (Sigma, #H3375), 0.2  
693 mM EGTA.KOH (Sigma, #E3889), 4 mM MgATP (Sigma, #A9187), 0.3 mM Na<sub>2</sub>GTP (Sigma, #G8877), 8 mM  
694 Phosphocreatine-Tris<sub>2</sub> (Sigma, #P1937) and 0.4% biocytin (Sigma, #B4261), equilibrated with 1 M KOH at pH 7.3.  
695 Recordings were performed using a Multiclamp 700B amplifier (Molecular Devices) and digitized using a Digidata 1440A  
696 and the Clampex 10 program suite (Molecular Devices). Cells were only accepted for analysis if the initial series  
697 resistance was less than 40 MΩ and did not change by more than 20% during the recording period. No corrections were  
698 made for the liquid junction potential. Intrinsic properties were obtained from JAM2+ cells labeled by AAV virus at a  
699 holding potential of -60 to -65 mV with the current-clamp internal. For optogenetic-assisted circuit mapping, voltage-clamp  
700 signals were filtered at 3 kHz and recorded with a sampling rate of 20 kHz. IPSCs were recorded at a holding potential of  
701 0 mV. Whole-cell patch-clamp recordings were obtained from JAM2+ cells labeled by AAV virus and unlabeled putative  
702 PYN or L4-5 SST+ cINs labeled by AAVPHP.s9e10.dTom (unpublished SST enhancer) in the same column with the  
703 voltage-clamp internal. To activate afferents expressing hChR2, blue light was transmitted from a collimated LED  
704 (Mightex) attached to the epifluorescence port of the upright microscope. 5 ms pulses of a fixed light intensity were  
705 directed to the slice in the recording chamber via a mirror coupled to the 40x objective. Flashes were delivered every 15s  
706 for a total of 10 trials. The LED output was driven by a transistor-transistor logic output from the Clampex software.  
707 Recordings were performed in the presence of 1 μM TTX and 1 mM 4-AP (Tocris). In some experiments, the IPSCs were  
708 confirmed with 10 μM SR95531 (Tocris, #1262). Data analysis was performed offline using the Clampfit module of  
709 pClamp (Molecular Devices). Individual waveforms from all trials per cell were averaged, and the averaged peak  
710 amplitude was analyzed.

#### 711 Statistical analysis

712 Statistical details of experiments can be found in the figure legends and supplementary tables. All statistical analyses  
713 were performed with hierarchical bootstrap<sup>83</sup>, linear mixed effect models (considering animal as random effect)<sup>84</sup> or one-  
714 way ANOVA. Mann Whitney test (such as ratios) or Wilcoxon signed rank test (such as two groups from the same  
715 animals) were used for animal level data. GraphPad Prism and Python were used to conduct statistical tests. \*p < 0.05, \*\*  
716 < 0.01, \*\*\* < 0.001, \*\*\*\* < 0.0001.

717

## 718 **ACKNOWLEDGEMENTS**

719 This work was supported by grants from the National Institutes of Health R01 NS081297, R37 MH071679, P01  
720 NS074972, UG3 MH120096, and the Simons Foundation Autism Research Initiative to G.F., NINDS P30 NS072030 to  
721 Harvard Medical School Neurobiology Imaging Facility, Quan Predoctoral Fellowship (FY22), Edward R. and Anne G.  
722 Lefler Center Predoctoral Fellowship (FY23, FY24) and Ryan Fellowship (FY23) to S.H.. We thank Dr. Emilia Favuzzi, Dr.  
723 Mark Andermann and Dionnet Bhatti for comments on the manuscript. We thank Dr. John Ngai, Dr. David A. Stafford, Dr.  
724 Susan M. Dymecki, Dr. David Ginty, Dr. Tanya L. Daigle, Dr. Bosiljka Tasic and Dr. Hongkui Zeng for generously sharing  
725 the genetic mouse strains. We thank Dr. Kimberly Ritola for sharing the rabies virus. We thank Dr. Gabrielle Pouchelon for  
726 sharing the VTK plasmid toolkit. We thank Dr. Jordane Dimidschstein and Sofi Vergara for sharing AAVPHP.s9e10.dTom  
727 enhancer AAV for SST targeting. We extend our sincere gratitude to Dr. Xindong Song for his invaluable guidance for the  
728 intrinsic imaging experiments. We thank John LeBlanc (HMS Machine Shop), Pavel Gorelik, and Dr. Ofer Mazor (HMS  
729 Research Instrumentation Core) for their assistance in engineering the *in vivo* imaging platform. We are grateful to Dr.  
730 Sergey Matveev and Dr. Utsab Khadka (Thorlabs) for their expertise and assistance with the two-photon microscopy  
731 setup. We thank Dr. Min Dai for discussion on transcriptomic data analysis. We thank all colleagues in the Fishell  
732 laboratory, Dr. Christopher D. Harvey, Dr. Anne Takesian, Dr. Daniel Polley, Dr. Bernardo Rudy, and Dr. Robert Machold  
733 for helpful discussion on this project over the years.

## 734 **AUTHOR CONTRIBUTION**

735 Conceptualization and methodology, S.H.; investigation, S.H., D.R., S.J.W., L.Z.; analysis, S.H., D.R.; resources -  
736 plasmids and AAV, Q.X., S.H.; resources - mouselines, D.A.S., T.L.D., B.T., H.Z.; writing - original draft, S.H.; writing -  
737 review and editing, G.F., L.A.I., S.J.W; supervision, G.F., L.A.I.; funding and resources, G.F..

738

- 740 1. Tremblay, R., Lee, S. & Rudy, B. GABAergic Interneurons in the Neocortex: From Cellular Properties to Circuits.  
741 *Neuron* **91**, 260–292 (2016).
- 742 2. Fishell, G. & Kepecs, A. Interneuron Types as Attractors and Controllers. *Annu. Rev. Neurosci.* **43**, 1–30 (2020).
- 743 3. Kepecs, A. & Fishell, G. Interneuron cell types are fit to function. *Nature* **505**, 318–326 (2014).
- 744 4. Zeng, H. What is a cell type and how to define it? *Cell* **185**, 2739–2755 (2022).
- 745 5. Rudy, B., Fishell, G., Lee, S. & Hjerling-Leffler, J. Three groups of interneurons account for nearly 100% of  
746 neocortical GABAergic neurons. *Dev. Neurobiol.* **71**, 45–61 (2011).
- 747 6. Ramón y Cajal, S. *Textura del sistema nervioso del hombre y de los vertebrados*. (Nicolás Moya, 1899).
- 748 7. Overstreet-Wadiche, L. & McBain, C. J. Neurogliaform cells in cortical circuits. *Nat. Rev. Neurosci.* **16**, 458–468  
749 (2015).
- 750 8. Armstrong, C., Krook-Magnuson, E. & Soltesz, I. Neurogliaform and Ivy Cells: A Major Family of nNOS Expressing  
751 GABAergic Neurons. *Front. Neural Circuits* **6**, 23 (2012).
- 752 9. Hodge, R. D. *et al.* Conserved cell types with divergent features in human versus mouse cortex. *Nature* **573**, 61–68  
753 (2019).
- 754 10. Tasic, B. *et al.* Shared and distinct transcriptomic cell types across neocortical areas. *Nature* **563**, 72–78 (2018).
- 755 11. Chittajallu, R., Pelkey, K. A. & McBain, C. J. Neurogliaform cells dynamically regulate somatosensory integration via  
756 synapse-specific modulation. *Nat. Neurosci.* **16**, 13–15 (2013).
- 757 12. Gouwens, N. W. *et al.* Integrated Morphoelectric and Transcriptomic Classification of Cortical GABAergic Cells. *Cell*  
758 **183**, 935–953.e19 (2020).
- 759 13. Kawaguchi, Y. & Kubota, Y. GABAergic cell subtypes and their synaptic connections in rat frontal cortex. *Cereb.*  
760 *Cortex* **7**, 476–486 (1997).
- 761 14. Oláh, S. *et al.* Output of neurogliaform cells to various neuron types in the human and rat cerebral cortex. *Front.*  
762 *Neural Circuits* **1**, 4 (2007).
- 763 15. Kawaguchi, Y., Karube, F. & Kubota, Y. Dendritic branch typing and spine expression patterns in cortical  
764 nonpyramidal cells. *Cereb. Cortex* **16**, 696–711 (2006).
- 765 16. Schuman, B. *et al.* Four Unique Interneuron Populations Reside in Neocortical Layer 1. *J. Neurosci.* **39**, 125–139  
766 (2019).
- 767 17. Turner, N. L. *et al.* Reconstruction of neocortex: Organelles, compartments, cells, circuits, and activity. *Cell* **185**,  
768 1082–1100.e24 (2022).
- 769 18. Tamás, G., Lorincz, A., Simon, A. & Szabadics, J. Identified sources and targets of slow inhibition in the neocortex.

- 770 *Science* **299**, 1902–1905 (2003).
- 771 19. Krimer, L. S. *et al.* Cluster analysis-based physiological classification and morphological properties of inhibitory  
772 neurons in layers 2-3 of monkey dorsolateral prefrontal cortex. *J. Neurophysiol.* **94**, 3009–3022 (2005).
- 773 20. Oláh, S. *et al.* Regulation of cortical microcircuits by unitary GABA-mediated volume transmission. *Nature* **461**, 1278–  
774 1281 (2009).
- 775 21. Jiang, X. *et al.* Principles of connectivity among morphologically defined cell types in adult neocortex. *Science* **350**,  
776 aac9462 (2015).
- 777 22. Simon, A., Oláh, S., Molnár, G., Szabadics, J. & Tamás, G. Gap-junctional coupling between neurogliaform cells and  
778 various interneuron types in the neocortex. *J. Neurosci.* **25**, 6278–6285 (2005).
- 779 23. Zsiros, V. & Maccaferri, G. Electrical coupling between interneurons with different excitable properties in the stratum  
780 lacunosum-moleculare of the juvenile CA1 rat hippocampus. *J. Neurosci.* **25**, 8686–8695 (2005).
- 781 24. Price, C. J. *et al.* Neurogliaform neurons form a novel inhibitory network in the hippocampal CA1 area. *J. Neurosci.*  
782 **25**, 6775–6786 (2005).
- 783 25. Yao, Z. *et al.* A high-resolution transcriptomic and spatial atlas of cell types in the whole mouse brain. *Nature* **624**,  
784 317–332 (2023).
- 785 26. Pfisterer, U. *et al.* Identification of epilepsy-associated neuronal subtypes and gene expression underlying  
786 epileptogenesis. *Nat. Commun.* **11**, 1–19 (2020).
- 787 27. Hodge, R. D. *et al.* Conserved cell types with divergent features in human versus mouse cortex. *Nature* **573**, 61–68  
788 (2019).
- 789 28. Abs, E. *et al.* Learning-Related Plasticity in Dendrite-Targeting Layer 1 Interneurons. *Neuron* **100**, 684–699.e6  
790 (2018).
- 791 29. Poorthuis, R. B. *et al.* Rapid Neuromodulation of Layer 1 Interneurons in Human Neocortex. *Cell Rep.* **23**, 951–958  
792 (2018).
- 793 30. Cohen-Kashi Malina, K. *et al.* NDNF interneurons in layer 1 gain-modulate whole cortical columns according to an  
794 animal's behavioral state. *Neuron* **109**, 2150–2164.e5 (2021).
- 795 31. Fan, L. Z. *et al.* All-Optical Electrophysiology Reveals the Role of Lateral Inhibition in Sensory Processing in Cortical  
796 Layer 1. *Cell* **180**, 521–535.e18 (2020).
- 797 32. Belén Pardi, M. *et al.* A thalamocortical top-down circuit for associative memory. *Science* **370**, 844–848 (2020).
- 798 33. Machold, R. *et al.* Id2 GABAergic interneurons comprise a neglected fourth major group of cortical inhibitory cells.  
799 *Elife* **12**, (2023).
- 800 34. Dimidschstein, J. *et al.* A viral strategy for targeting and manipulating interneurons across vertebrate species. *Nat.*

- 801 *Neurosci.* **19**, 1743–1749 (2016).
- 802 35. Kawaguchi, Y. Physiological subgroups of nonpyramidal cells with specific morphological characteristics in layer II/III  
803 of rat frontal cortex. *J. Neurosci.* **15**, 2638–2655 (1995).
- 804 36. Szabadics, J., Tamás, G. & Soltesz, I. Different transmitter transients underlie presynaptic cell type specificity of  
805 GABA<sub>A</sub>,slow and GABA<sub>A</sub>,fast. *Proc. Natl. Acad. Sci. U. S. A.* **104**, 14831–14836 (2007).
- 806 37. Kim, J. C. *et al.* Linking genetically defined neurons to behavior through a broadly applicable silencing allele. *Neuron*  
807 **63**, 305–315 (2009).
- 808 38. Fu, Y. *et al.* A cortical circuit for gain control by behavioral state. *Cell* **156**, 1139–1152 (2014).
- 809 39. Pakan, J. M. *et al.* Behavioral-state modulation of inhibition is context-dependent and cell type specific in mouse  
810 visual cortex. *Elife* **5**, (2016).
- 811 40. Dipoppa, M. *et al.* Vision and Locomotion Shape the Interactions between Neuron Types in Mouse Visual Cortex.  
812 *Neuron* **98**, 602–615.e8 (2018).
- 813 41. Millman, D. J. *et al.* VIP interneurons in mouse primary visual cortex selectively enhance responses to weak but  
814 specific stimuli. *Elife* **9**, (2020).
- 815 42. Ibrahim, L. A. *et al.* Bottom-up inputs are required for establishment of top-down connectivity onto cortical layer 1  
816 neurogliaform cells. *Neuron* **109**, 3473–3485.e5 (2021).
- 817 43. Huang, S., Wu, S. J., Sansone, G., Ibrahim, L. A. & Fishell, G. Layer 1 neocortex: Gating and integrating  
818 multidimensional signals. *Neuron* **112**, 184–200 (2024).
- 819 44. Wall, N. R. *et al.* Brain-Wide Maps of Synaptic Input to Cortical Interneurons. *J. Neurosci.* **36**, 4000–4009 (2016).
- 820 45. Yao, S. *et al.* A whole-brain monosynaptic input connectome to neuron classes in mouse visual cortex. *Nat. Neurosci.*  
821 **26**, 350–364 (2023).
- 822 46. Oh, S. W. *et al.* A mesoscale connectome of the mouse brain. *Nature* **508**, 207–214 (2014).
- 823 47. Schuman, B., Dellal, S., Prönnke, A., Machold, R. & Rudy, B. Neocortical Layer 1: An Elegant Solution to Top-Down  
824 and Bottom-Up Integration. *Annu. Rev. Neurosci.* **44**, 221–252 (2021).
- 825 48. Harris, K. D. & Mrsic-Flogel, T. D. Cortical connectivity and sensory coding. *Nature* **503**, 51–58 (2013).
- 826 49. Sakata, S. & Harris, K. D. Laminar structure of spontaneous and sensory-evoked population activity in auditory  
827 cortex. *Neuron* **64**, 404–418 (2009).
- 828 50. Voelcker, B., Pancholi, R. & Peron, S. Transformation of primary sensory cortical representations from layer 4 to layer  
829 2. *Nat. Commun.* **13**, 5484 (2022).
- 830 51. Petersen, C. C. H. & Crochet, S. Synaptic computation and sensory processing in neocortical layer 2/3. *Neuron* **78**,  
831 28–48 (2013).

- 832 52. Barth, A. L. & Poulet, J. F. A. Experimental evidence for sparse firing in the neocortex. *Trends Neurosci.* **35**, 345–355  
833 (2012).
- 834 53. Bugeon, S. *et al.* A transcriptomic axis predicts state modulation of cortical interneurons. *Nature* **607**, 330–338  
835 (2022).
- 836 54. Hartung, J., Schroeder, A., Pérez Vázquez, R. A., Poorthuis, R. B. & Letzkus, J. J. Layer 1 NDNF interneurons are  
837 specialized top-down master regulators of cortical circuits. *Cell Rep.* **43**, 114212 (2024).
- 838 55. Lee, S., Kruglikov, I., Huang, Z. J., Fishell, G. & Rudy, B. A disinhibitory circuit mediates motor integration in the  
839 somatosensory cortex. *Nat. Neurosci.* **16**, 1662–1670 (2013).
- 840 56. Pfeffer, C. K., Xue, M., He, M., Huang, Z. J. & Scanziani, M. Inhibition of inhibition in visual cortex: the logic of  
841 connections between molecularly distinct interneurons. *Nat. Neurosci.* **16**, 1068–1076 (2013).
- 842 57. Polack, P.-O., Friedman, J. & Golshani, P. Cellular mechanisms of brain state-dependent gain modulation in visual  
843 cortex. *Nat. Neurosci.* **16**, 1331–1339 (2013).
- 844 58. Erlander, M. G., Tillakaratne, N. J., Feldblum, S., Patel, N. & Tobin, A. J. Two genes encode distinct glutamate  
845 decarboxylases. *Neuron* **7**, 91–100 (1991).
- 846 59. Pazarlar, B. A. *et al.* Expression profile of synaptic vesicle glycoprotein 2A, B, and C paralogues in temporal  
847 neocortex tissue from patients with temporal lobe epilepsy (TLE). *Mol. Brain* **15**, 45 (2022).
- 848 60. Janz, R. & Südhof, T. C. SV2C is a synaptic vesicle protein with an unusually restricted localization: anatomy of a  
849 synaptic vesicle protein family. *Neuroscience* **94**, 1279–1290 (1999).
- 850 61. Dunn, A. R. *et al.* Synaptic vesicle glycoprotein 2C (SV2C) modulates dopamine release and is disrupted in  
851 Parkinson disease. *Proc. Natl. Acad. Sci. U. S. A.* **114**, E2253–E2262 (2017).
- 852 62. Bucher, M. L. *et al.* Synaptic vesicle glycoprotein 2C enhances vesicular storage of dopamine and counters  
853 dopaminergic toxicity. *European Journal of Neuroscience* **59**, 2483–2501 (2024).
- 854 63. Schuster, A. *et al.* SpermBase: A Database for Sperm-Borne RNA Contents. *Biol. Reprod.* **95**, 99 (2016).
- 855 64. Xiong, Z. *et al.* Ultrasensitive Ribo-seq reveals translational landscapes during mammalian oocyte-to-embryo  
856 transition and pre-implantation development. *Nat. Cell Biol.* **24**, 968–980 (2022).
- 857 65. Pouchelon, G. *et al.* A versatile viral toolkit for functional discovery in the nervous system. *Cell Rep Methods* **2**,  
858 100225 (2022).
- 859 66. Zhang, Y. *et al.* Fast and sensitive GCaMP calcium indicators for imaging neural populations. *Nature* **615**, 884–891  
860 (2023).
- 861 67. Song, X. *et al.* Mesoscopic landscape of cortical functions revealed by through-skull wide-field optical imaging in  
862 marmoset monkeys. *Nat. Commun.* **13**, 2238 (2022).



- 863 68. Brainard, D. H. The Psychophysics Toolbox. *Spat. Vis.* **10**, 433–436 (1997).
- 864 69. Pelli, D. G. The VideoToolbox software for visual psychophysics: transforming numbers into movies. *Spat. Vis.* **10**,  
865 437–442 (1997).
- 866 70. Augustinaite, S. & Kuhn, B. Intrinsic optical signal imaging and targeted injections through a chronic cranial window of  
867 a head-fixed mouse. *STAR Protoc* **2**, 100779 (2021).
- 868 71. Schindelin, J. *et al.* Fiji: an open-source platform for biological-image analysis. *Nat. Methods* **9**, 676–682 (2012).
- 869 72. Syeda, A. *et al.* Facemap: a framework for modeling neural activity based on orofacial tracking. *Nat. Neurosci.* **27**,  
870 187–195 (2024).
- 871 73. Mathôt, S. *et al.* A simple way to reconstruct pupil size during eye blinks. *Retrieved from* **10**, m9 (2013).
- 872 74. Pachitariu, M. *et al.* Suite2p: beyond 10,000 neurons with standard two-photon microscopy. *bioRxiv* 061507 (2017)  
873 doi:10.1101/061507.
- 874 75. Chen, T.-W. *et al.* Ultrasensitive fluorescent proteins for imaging neuronal activity. *Nature* **499**, 295–300 (2013).
- 875 76. Dana, H. *et al.* High-performance calcium sensors for imaging activity in neuronal populations and  
876 microcompartments. *Nat. Methods* **16**, 649–657 (2019).
- 877 77. Pettit, N. L., Yuan, X. C. & Harvey, C. D. Hippocampal place codes are gated by behavioral engagement. *Nat.*  
878 *Neurosci.* **25**, 561–566 (2022).
- 879 78. Pettit, N. L., Yap, E.-L., Greenberg, M. E. & Harvey, C. D. Fos ensembles encode and shape stable spatial maps in  
880 the hippocampus. *Nature* **609**, 327–334 (2022).
- 881 79. Montijn, J. S., Vinck, M. & Pennartz, C. M. A. Population coding in mouse visual cortex: response reliability and  
882 dissociability of stimulus tuning and noise correlation. *Front. Comput. Neurosci.* **8**, 61783 (2014).
- 883 80. Reardon, T. R. *et al.* Rabies Virus CVS-N2c( $\Delta$ G) Strain Enhances Retrograde Synaptic Transfer and Neuronal  
884 Viability. *Neuron* **89**, 711–724 (2016).
- 885 81. Pouchelon, G. *et al.* The organization and development of cortical interneuron presynaptic circuits are area specific.  
886 *Cell Rep.* **37**, 109993 (2021).
- 887 82. Ting, J. T. *et al.* Preparation of Acute Brain Slices Using an Optimized N-Methyl-D-glucamine Protective Recovery  
888 Method. *J. Vis. Exp.* (2018) doi:10.3791/53825.
- 889 83. Saravanan, V., Berman, G. J. & Sober, S. J. Application of the hierarchical bootstrap to multi-level data in  
890 neuroscience. *Neuron Behav Data Anal Theory* **3**, (2020).
- 891 84. Yu, Z. *et al.* Beyond t test and ANOVA: applications of mixed-effects models for more rigorous statistical analysis in  
892 neuroscience research. *Neuron* **110**, 21–35 (2022).
- 893 85. Krienen, F. M. *et al.* Innovations present in the primate interneuron repertoire. *Nature* **586**, 262 (2020).

894 86. Valero, M. *et al.* Sleep down state-active ID2/Nkx2.1 interneurons in the neocortex. *Nat. Neurosci.* **24**, 401–411  
895 (2021).

896

Figure 1

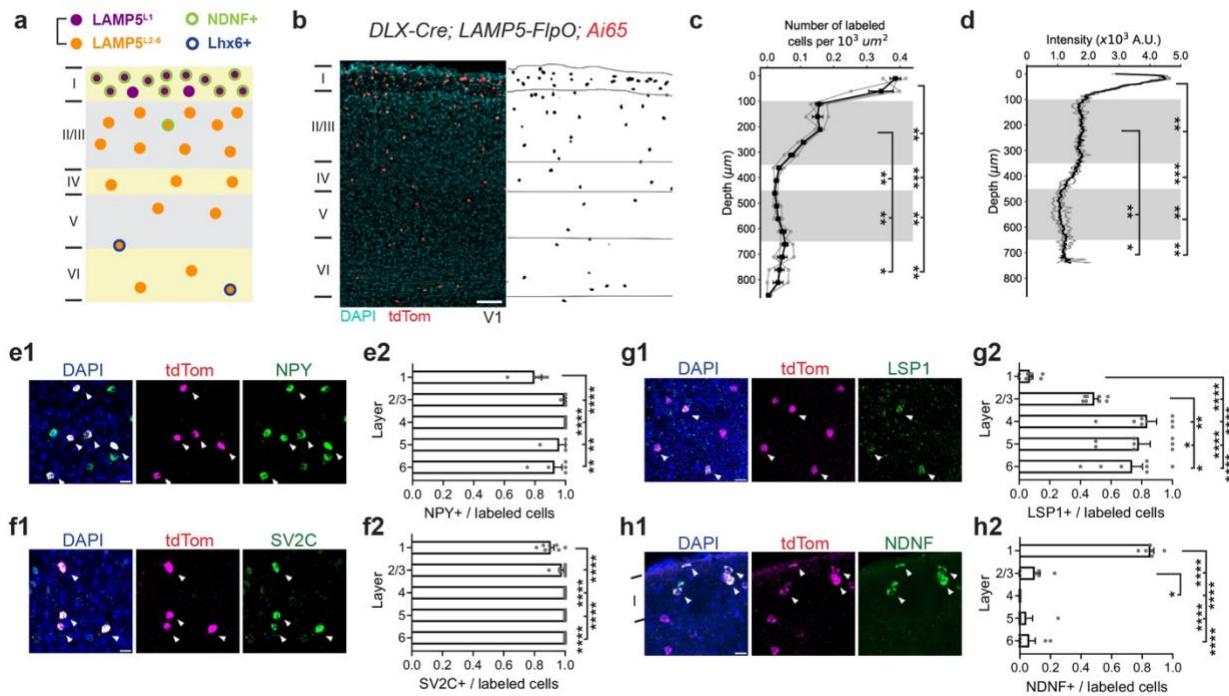


Figure 1. *DLX-Cre; LAMP5-FlpO* targets all LAMP5+ cINs.

(a) Schematic illustration of the distribution of LAMP5+ cINs in V1, indicating their various subtypes.

(b) Example image of *DLX-Cre; LAMP5-FlpO; Ai65(RCFL-tdT)* genetic labeling in V1 showing the distribution of LAMP5+ cINs (left) and segmented cell bodies (right). Scale bar = 100 μm.

(c) Quantification for the number of labeled cells per 10<sup>3</sup> μm<sup>2</sup> and (d) the intensity of labeled neurites in 10<sup>3</sup> arbitrary units (A.U.) across cortical layers. Gray indicates L2/3 and L5. The 40 μm thick coronal V1 sections were divided into 50 μm vertical bands for cell density measurement. Each gray line represents data from an individual animal.

(e-h) Representative RNAscope assays images in V1 taken with confocal microscopy and bar plots quantifying the ratio of marker gene-positive cells to all tdTom labeled cells in each cortical layer. Each panel displays an overlay figure (left) with nuclei dye DAPI (in blue), tdTom-labeled cells from *DLX-Cre; LAMP5-FlpO; Ai65(RCFL-tdT)* (middle, in red), and the marker gene expression detected by RNAscope assay (right, in green). Scale bar = 20 μm. Each dot represents data from one coronal V1 section. Arrow indicates tdTom and marker gene co-localized cells. (e1-e2) NPY; (f1-f2) SV2C; (g1-g2) LSP1; (h1-h2) NDNF. While NPY is a classical marker for identifying neurogliaform cells in rodents, it is not exclusively restricted to LAMP5+ cINs. Moreover, although LSP1 serves as a specific marker gene for the *Lamp5/Lsp1* cluster, it is expressed in only half of the neurons within this population. Data from N = 3 animals. Error bar represents SEM. Repeated measures ANOVA (c-d, g2-h2) or mixed-effects model (e2) followed by uncorrected Fisher's LSD were used for testing statistical significance. See supplementary data 1 - Table 1 for statistics.

Figure 2

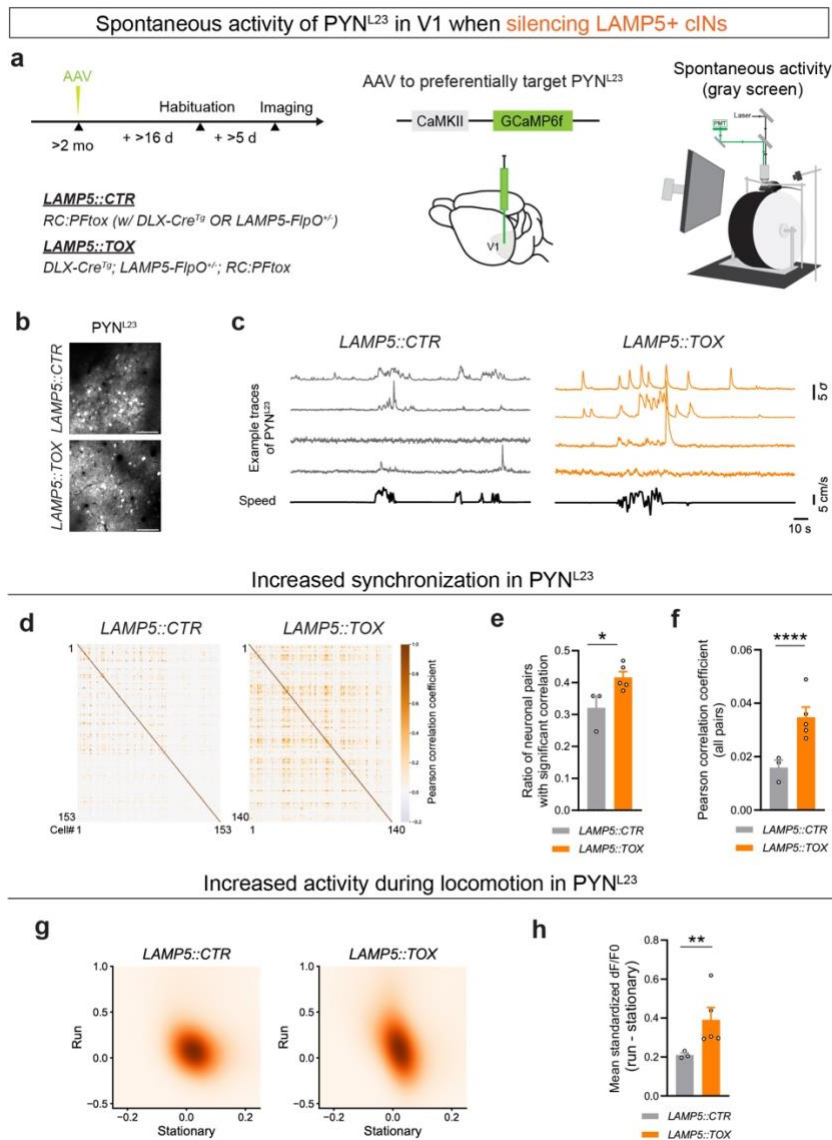


**Figure 2. LAMP5+ cIN silencing results in increased spontaneous activity of PYN<sup>L23</sup> in V1.**

(a) (left) The experimental animals (*LAMP5::TOX*) were generated by crossing the *DLX-Cre; LAMP5-FlpO* mouse model with *RC:PFtoX*, specifically, *DLX-Cre<sup>Tg</sup>; LAMP5-FlpO<sup>+/+</sup>; RC:PFtoX<sup>Flox/+, Frt/+</sup>*. Controls (*LAMP5::CTR*) were mice lacking Cre and/or FlpO (either one or both negative) while still carrying the *RC:PFtoX<sup>Flox/+, Frt/+</sup>* genotype. No notable differences were observed among different control genotypes. (middle) To visualize PYN<sup>L23</sup> activity, AAV9.CaMKII.GCaMP6f.WPRE.SV40 was injected into V1 during the cranial window implantation surgery to express GCaMP6f preferentially in PYN<sup>L23</sup>. Intrinsic imaging (refer to Methods) was used to confirm the V1 location in each animal before proceeding with *in vivo* two-photon calcium imaging experiments. (right) Illustration of the experimental setup during the spontaneous activity recordings. The animal was presented with a gray screen (uniform mean luminance) during two-photon imaging of the GCaMP signal.

(b) Example images from the maximum intensity projection of the two-photon imaging experiments, showing GCaMP6f expression within L2/3 of V1 in *LAMP5::CTR* (upper) and *LAMP5::TOX* (bottom). Scale bar = 100 μm.

(c) Example traces from spontaneous activity recordings in both *LAMP5::CTR* (left) and *LAMP5::TOX* (right). The top four traces in each set (gray for *LAMP5::CTR* and orange for *LAMP5::TOX*) represent the smoothed standardized dF/F0 activity of four randomly chosen neurons during a randomly selected time interval for representation. The bottom trace (in black) in each set shows the corresponding locomotion speed of the animal (measured in cm/s).

(d) Example heatmap showing Pearson's correlation coefficient of neuron pairs from a single imaging session using *LAMP5::CTR* (left) or *LAMP5::TOX* (right).

(e) Bar plot showing ratio of significantly ( $p < 0.05$ ) correlated pairs out of all neuron pairs with shuffling (refer to Methods) in *LAMP5::CTR* (gray) and *LAMP5::TOX* (orange).

(f) Bar plot showing Pearson's correlation coefficient of all neuron pairs in *LAMP5::CTR* (gray) and *LAMP5::TOX* (orange).

(g) Averaged spontaneous standardized dF/F0 activity for each neuron during either stationary (speed  $\leq 1$  cm/s) or running (speed  $> 1$  cm/s) period for *LAMP5::CTR* (left) and *LAMP5::TOX* (right) groups. The data are fit with a Gaussian kernel for visualization.

(h) Bar plot showing the differences in mean standardized dF/F0 activity between running and stationary period, obtained by subtracting the latter from the former, for *LAMP5::CTR* (gray) and *LAMP5::TOX* (orange).

Error bar represents SEM. Each dot represents the (averaged) result from an individual animal. Mann-Whitney test (e) and hierarchical bootstrap (f,h-i) were used for testing statistical significance. See supplementary data 1 - Table 2 for statistics.

Figure 3

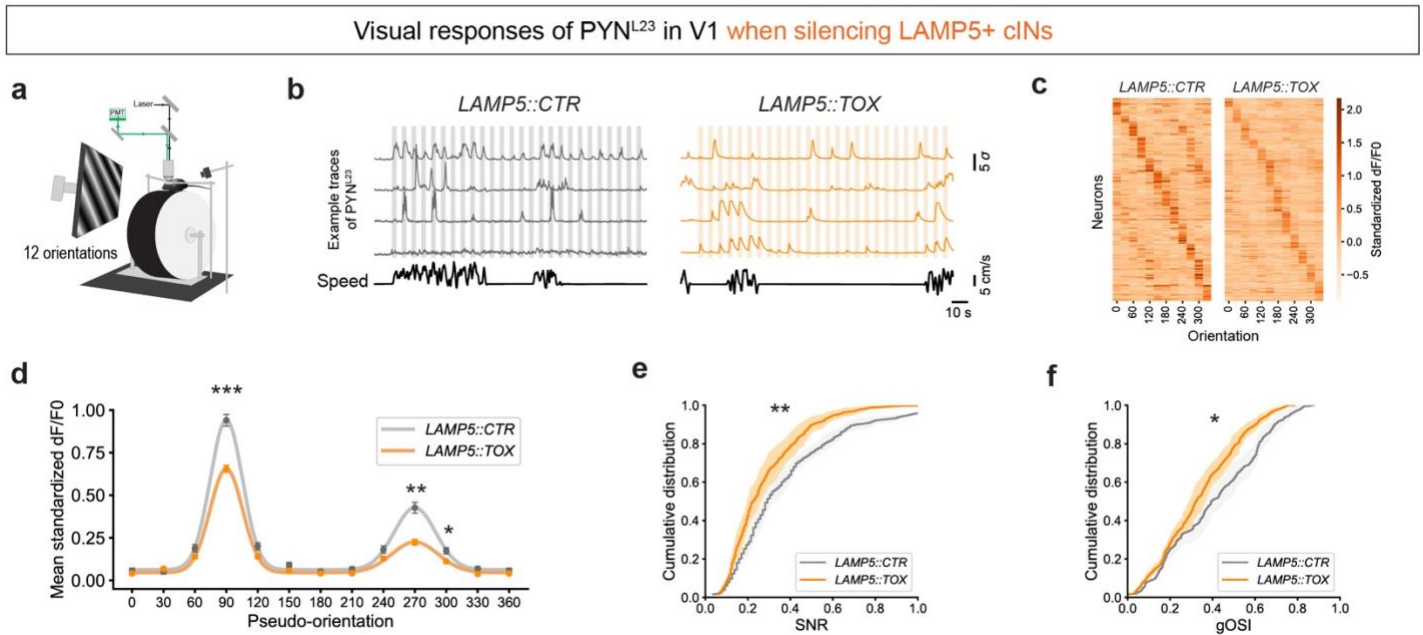


**Figure 3 - LAMP5+ cIN silencing results in impaired visual response properties of PYN<sup>L23</sup> in V1.**

(a) Illustration of the experimental setup during the recording of visual responses. The animal was presented with moving gratings on the screen, while the GCaMP signal in PYN<sup>L23</sup> was imaged with two-photon microscopy. Each trial was 6s, consisting of 2s full-field moving gratings with orientations displayed randomly, a fixed contrast (80%), spatial frequency (0.04 cpd) and temporal frequency (1 Hz). 4s inter-stimulus-intervals of gray screen (mean luminance) was presented. 12 orientations were examined: 0°, 30°, 60°, 90°, 120°, 150°, 180°, 210°, 240°, 270°, 300°, 330°.

(b) Example traces of PYN<sup>L23</sup> responses from the *LAMP5::CTR* (gray) or *LAMP5::TOX* (orange) mice. The top four traces in each set represent the standardized dF/F<sub>0</sub> activity (smoothed for representation) of four randomly chosen neurons during a randomly selected time interval. The bottom trace (in black) in each set showed the corresponding locomotion speed of the animal (measured in cm/s). Colored fill (gray or orange) indicates the presence of moving gratings.

(c) Heatmap showing averaged visual responses to various tested orientations (columns) of all recorded neurons (rows) sorted by their preferred orientation for *LAMP5::CTR* (left) and *LAMP5::TOX* (right).

(d) Averaged visual responses to orientations (pseudo-90° indicates the preferred orientation for a neuron) in *LAMP5::CTR* (gray) and *LAMP5::TOX* (orange).

(e) Cumulative ratio of signal-noise-ratio (SNR) for *LAMP5::CTR* (gray) and *LAMP5::TOX* (orange).

(f) Cumulative ratio of signal correlation of visual responses for *LAMP5::CTR* (gray) and *LAMP5::TOX* (orange).

(g) Cumulative ratio of global orientation selective index (gOSI) for *LAMP5::CTR* (gray) and *LAMP5::TOX* (orange).

Error bar represents SEM. Hierarchical bootstrap was used for testing statistical significance. See supplementary data 1 - Table 3 for statistics.

Figure 4

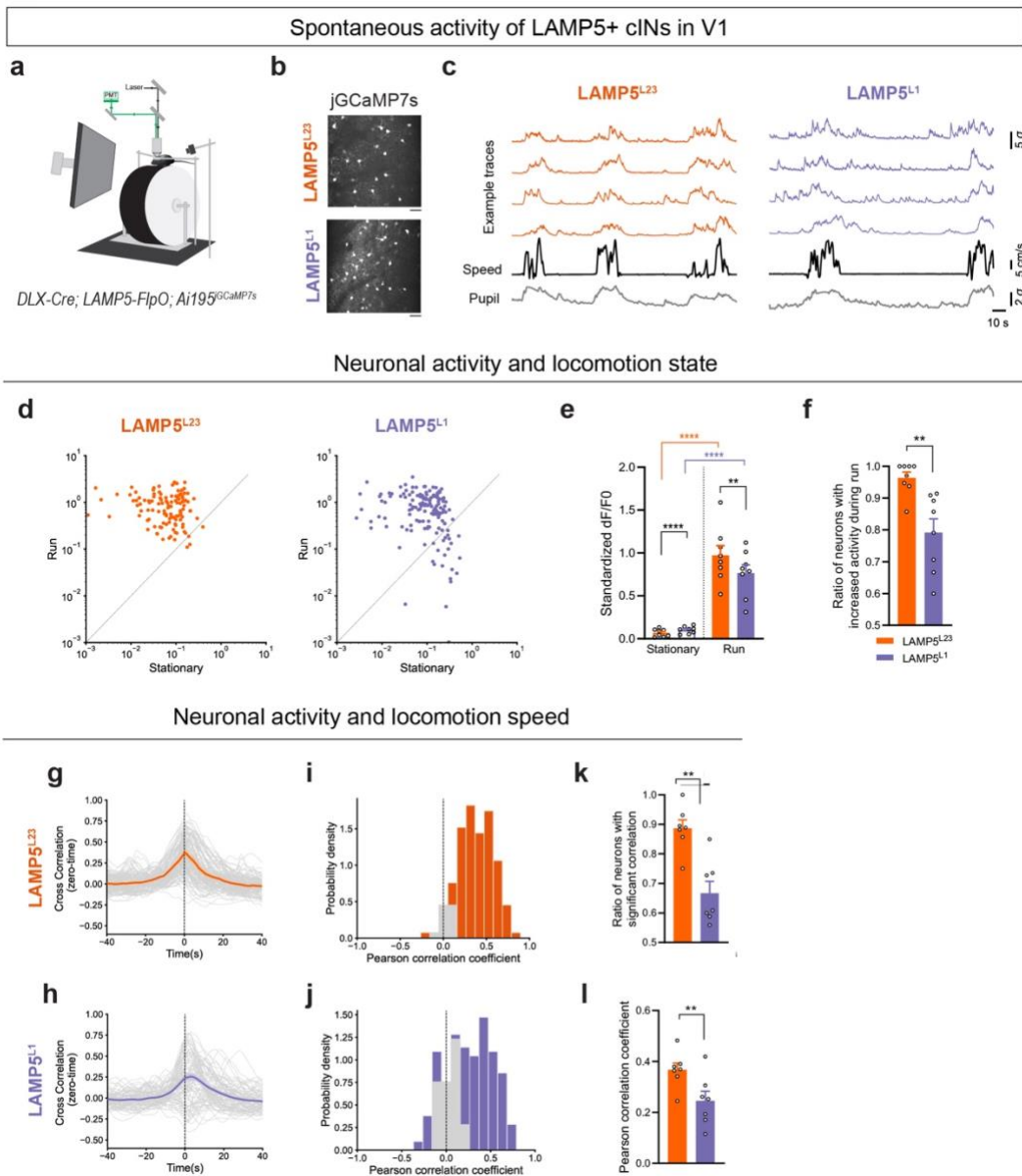


Figure 4. Spontaneous activity of LAMP5+ cINs is correlated with locomotion speed.

(a) Illustration of the experimental setup during the spontaneous activity recordings. The animal was presented with a gray screen (mean luminance) while the GCaMP signal was imaged with two-photon microscopy.

(b) A representative mean projection image from a two-photon recording session in L2/3 (upper) or L1 (bottom) LAMP5+ cINs in V1 of *DLX-Cre; LAMP5-FlpO; Ai195<sup>jGCaMP7s</sup>*.

(c) Example traces from spontaneous activity recordings in LAMP5<sup>L23</sup> (left, in orange) and LAMP5<sup>L1</sup> (right, in purple). The top four traces represent the standardized dF/F0 activity of four randomly chosen neurons during a randomly selected time interval. The activity traces shown here are smoothed for representation. The black trace indicates the animal's locomotion speed (in cm/s), and the gray trace shows the z-scored pupil size, both measured concurrently.

(d) Scatter plot showing the mean standardized dF/F0 during stationary and running periods for LAMP5<sup>L23</sup> (left, in orange) and LAMP5<sup>L1</sup> (right, in purple). Each dot represents a neuron.

(e) Bar plot showing the mean standardized dF/F0 during stationary (white bar) and run (color filled bar) periods for LAMP5<sup>L23</sup> (orange) and LAMP5<sup>L1</sup> (purple).

(f) Bar plot showing ratio of neurons with increased activity during running periods.

(g-h) Zero-time cross-correlation analysis of neuronal activity between (g) LAMP5<sup>L23</sup> (orange) or (h) LAMP5<sup>L1</sup> (purple), and locomotion speed.

(i-j) Histogram of Pearson's correlation coefficient (same as cross-correlation value at zero-time) of (i) LAMP5<sup>L23</sup> (orange) or (j) LAMP5<sup>L1</sup> (purple) activity and locomotion speed. Gray bars represent pairs with no significant correlation and colored bars represent pairs with significant correlation, determined by comparing against shuffled time series for each pair for 1000 times (refer to Methods).

(k) Bar plot showing ratio of neurons with significant correlation between the spontaneous activity and locomotion speed for LAMP5<sup>L23</sup> (orange) or LAMP5<sup>L1</sup> (purple).

(l) Bar plot showing Pearson's correlation coefficient of the spontaneous activity and locomotion speed for LAMP5<sup>L23</sup> (orange) or LAMP5<sup>L1</sup> (purple). Error bar represents SEM. Each dot in the bar plots represents data from an individual mouse. Mann-Whitney test (f,k), mixed linear model regression (e) and hierarchical bootstrap (l) were used for testing statistical significance. See supplementary data 1 - Table 4 for statistics.

Figure 5

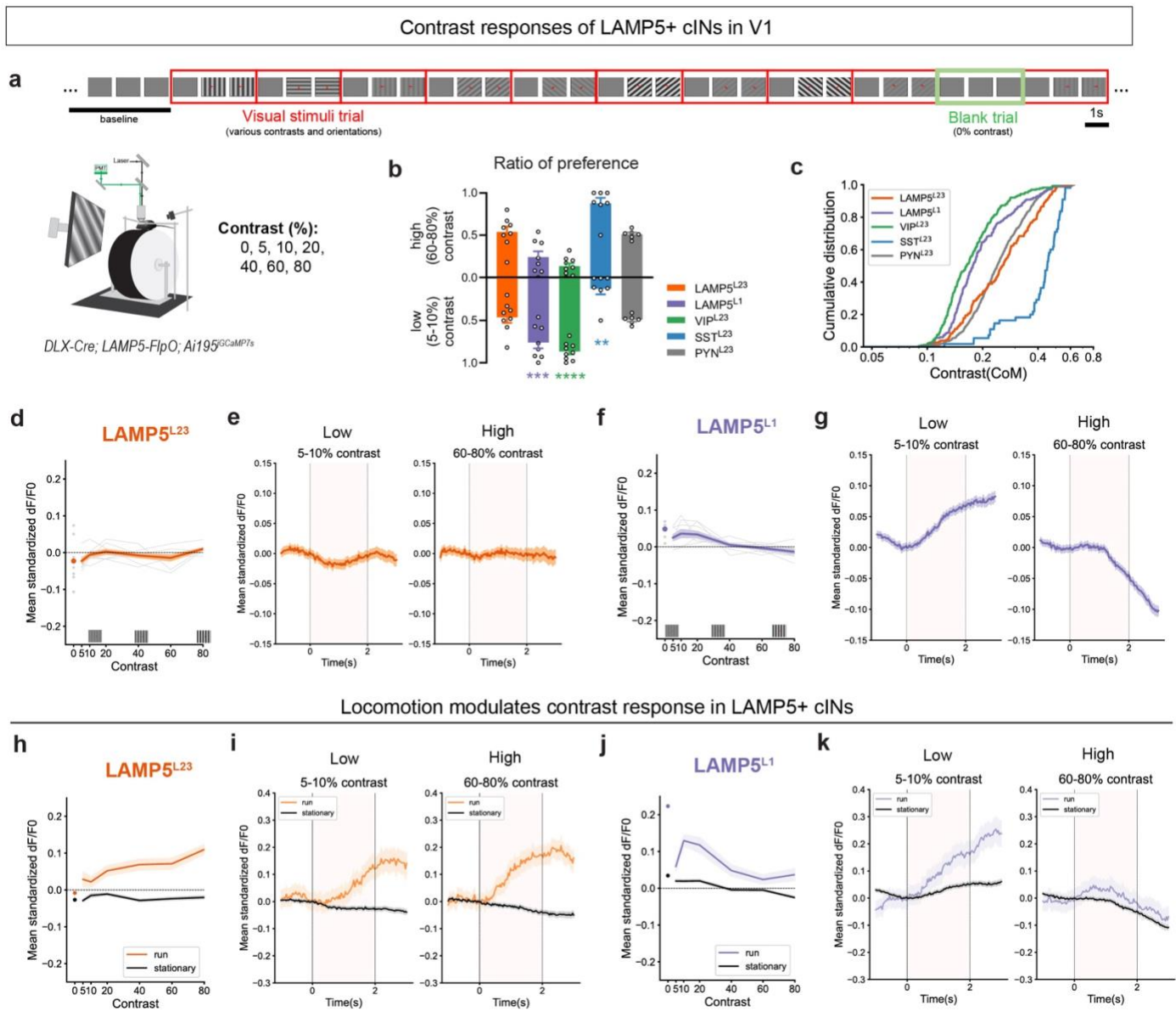


Figure 5. Visual responses and their modulation by locomotion are distinct in LAMP5<sup>L23</sup> and LAMP5<sup>L1</sup>.

(a) Illustration of the experimental trial design. After a baseline of 10 s with the gray screen, mice were presented with random 3s visual stimuli trials which each had 2s of full-screen moving gratings with variable contrast and orientations in each trial. 1s of inter-stimulus-interval was used with the gray screen. Six contrast levels (5%, 10%, 20%, 40%, 60% and 80%) and eight orientations (every 45°) were included in the task and each combination was randomly repeated for 15 trials. In addition, we included blank trials (0% contrast) randomly. Each blank trial consisted of 3s of gray screen.

(b) Ratio of high (60-80%) or low (5-10%) contrast preferring neurons in LAMP5<sup>L23</sup> (orange), LAMP5<sup>L1</sup> (purple), VIP<sup>L23</sup> (green), SST<sup>L23</sup> (blue) and PYN<sup>L23</sup> (gray). Each dot represents data from an individual animal. VIP<sup>L23</sup>/SST<sup>L23</sup> results were from *Germline-Cre*; *VIP-FlpO/SST-FlpO*; *Ai195* mice (*Ai195* is an intersectional reporter and this converts them into a Flp-reporter). PYN<sup>L23</sup> results were from TOX-control animals with AAV.GCaMP6f.

(c) Cumulative ratio of the center of mass in contrast response for each neuron in LAMP5<sup>L23</sup> (orange), LAMP5<sup>L1</sup> (purple), VIP<sup>L23</sup> (green), SST<sup>L23</sup> (blue) and PYN<sup>L23</sup> (gray).

(d) Visual responses at various contrast levels in LAMP5<sup>L23</sup> population.

(e) Averaged response trace in (left) low (5-10%) or (right) high (60-80%) contrasts for LAMP5<sup>L23</sup>.

(f) Visual responses at various contrast levels in LAMP5<sup>L1</sup> population.

(g) Averaged response trace in (left) low (5-10%) or (right) high (60-80%) contrasts for LAMP5<sup>L1</sup>.

(h) Visual responses at various contrast levels in LAMP5<sup>L23</sup> population during running (orange) or stationary (black) trials.

(i) Averaged response trace in (left) low (5-10%) or (right) high (60-80%) contrasts for LAMP5<sup>L23</sup> during running (orange) or stationary (black) trials.

(j) Visual responses at various contrast levels in LAMP5<sup>L1</sup> population during running (purple) or stationary (black) trials.

(k) Averaged response trace in (left) low (5-10%) or (right) high (60-80%) contrasts for LAMP5<sup>L1</sup> during running (purple) or stationary (black) trials.

In (d,f,h,i,j), each gray line and dot represent averaged data from an animal, while color line represents mean and SEM from all neurons. Responses at 0% contrast ('blank trial') were indicated by dot. In (e,g,i,k), moving gratings were presented between 0-2 s indicated by dashed gray vertical lines. The color lines represent mean and SEM from all animals. Mann Whitney test (b) and mixed linear model regression (d,f,h,i,j) were used for testing statistical significance. See supplementary data 1 - Table 5 for statistics.

Figure 6

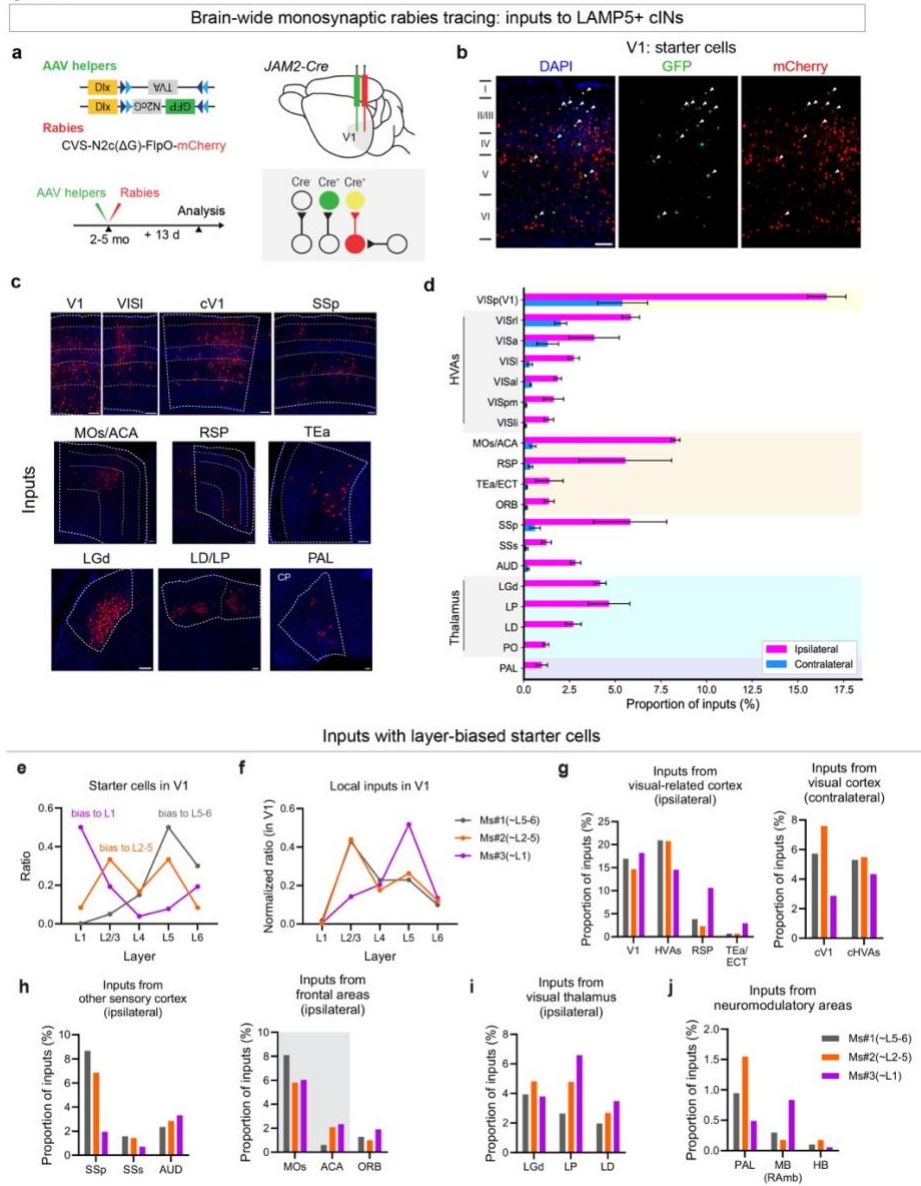


**Figure 6. Brain-wide monosynaptic inputs to LAMP5+ cINs reveal layer-dependent circuit connectivity of LAMP5+ cINs.**

(a) Experimental design of rabies retrograde tracing from LAMP5+ cINs in V1. Helper AAVs, AAV1.Dlx.DIO.TVA and AAV1.DLX.DIO.GFP.N2cG (green), were co-injected with EnVA-pseudotyped CVS-N2c(ΔG)-FlpO-mCherry rabies virus (red) into V1 of *JAM2-Cre* mice. Rabies tracing patterns were analyzed 13 days post-infection. GFP+ cells represent N2cG protein expression, while mCherry+ cells indicate presynaptically traced neurons. Cells positive for both GFP and mCherry were identified as starter cells.

(b) Example images showing starter cells in V1 (white arrow). Scale bar = 100 μm.

(c) Example images showing brain regions with significant inputs. Scale bar = 100 μm.

(d) Presynaptic inputs to LAMP5+ cINs in V1 were quantified as the percentage of rabies traced cells in each region out of the total number of cells labeled in the brain. Regions with >1% of inputs are included in the plot. Inputs from the ipsilateral side are colored in magenta, while those from the contralateral side are in blue.

(e) Starter cell layer distribution for 3 experimental repeats, Ms#1 (gray) had starter cells biased to deep layers L5-6, Ms#2 (orange) had starter cells biased to middle layers L2-5, while Ms#3 (purple) had starter cells biased to L1.

(f) Local inputs across cortical layers normalized to total local inputs (mCherry+, GFP- cells in V1) in V1 for 3 experimental repeats.

(g-j) Inputs from ipsilateral visual areas, contralateral visual areas, ipsilateral non-visual sensory areas, ipsilateral motor and frontal areas, ipsilateral visual thalamus, and putative neuromodulatory areas, such as PAL (putative cholinergic projection neurons in pallidum), MB (Ramb) (putative serotonergic neurons) and HB (putative noradrenergic neurons) for 3 experimental repeats.

The error bars represent SEM. Data was collected from N=3 animals.

Abbreviations: ACA: anterior cingulate area, AUD: auditory areas, cV1: contralateral primary visual area, cHVAs: contralateral higher-order visual areas, ECT: ectorrhinal area, HB: hindbrain, HVAs: higher-order visual areas, LD: lateral dorsal nucleus of thalamus, LGd: dorsal part of the lateral geniculate complex, LP: lateral posterior nucleus of the thalamus, MB: midbrain, MOs: secondary motor area, ORB: orbital area, PAL: pallidum, PO: posterior complex of the thalamus, RAmB: midbrain raphe nuclei, RSP: retrosplenial area, SSs: supplemental somatosensory area, SSp: primary somatosensory area, TEa: temporal association area, VISa: anterior area, VISal: anterolateral visual area, VISl: lateral visual area, VISli: laterointermediate area, VISpm: posteromedial visual area, VISp(V1): primary visual area, VISrl: rostromedial visual area.



## Supplementary Files

This is a list of supplementary files associated with this preprint. Click to download.

- [Supplementarydata.pdf](#)